JGR Atmospheres

RESEARCH ARTICLE
10.1029/2022JD038097

Special Section:
SOUTHTRAC-GW: An airborne field campaign to explore gravity wave dynamics at the world's strongest hotspot

Non-Orographic Gravity Waves and Turbulence Caused by Merging Jet Streams

W. Woiwode[1], A. Dörnbrack[2], M. Geldenhuys[3,4], F. Friedl-Vallon[1], A. Giez[5], T. Gulde[1], M. Höpfner[1], S. Johansson[1], B. Kaifler[2], A. Kleinert[1], L. Krasauskas[3], E. Kretschmer[1], G. Maucher[1], T. Neubert[6], H. Nordmeyer[1], C. Piesch[1], P. Preusse[3], M. Rapp[2,7], M. Riese[3], U. Schumann[2], and J. Ungermann[3]

[1]Institute of Meteorology and Climate Research, Karlsruhe Institute of Technology (KIT), Karlsruhe, Germany, [2]Deutsches Zentrum für Luft- und Raumfahrt, Institut für Physik der Atmosphäre (DLR-IPA), Oberpfaffenhofen, Germany, [3]Institute of Energy and Climate Research—Stratosphere (IEK-7), Forschungszentrum Jülich (FZJ), Jülich, Germany, [4]South African Weather Service, Pretoria, South Africa, [5]Deutsches Zentrum für Luft- und Raumfahrt, Einrichtung Flugexperimente (DLR-FX), Oberpfaffenhofen, Germany, [6]Zentralinstitut für Engineering, Elektronik und Analytik-Systeme der Elektronik (ZEA-2), Forschungszentrum Jülich (FZJ), Jülich, Germany, [7]Meteorologisches Institut München, Ludwig-Maximilians-Universität München, Munich, Germany

Abstract Jet streams are important sources of non-orographic internal gravity waves and clear air turbulence (CAT). We analyze non-orographic gravity waves and CAT during a merger of the polar front jet stream (PFJ) with the subtropical jet stream (STJ) above the southern Atlantic. Thereby, we use a novel combination of airborne observations covering the meso-scale and turbulent scale in combination with high-resolution deterministic short-term forecasts. Coherent phase lines of temperature perturbations by gravity waves stretching along a highly sheared tropopause fold are simulated by the ECMWF IFS (integrated forecast system) forecasts. During the merging event, the PFJ reverses its direction from approximately antiparallel to parallel with respect to the STJ, going along with strong wind shear and horizontal deformation. Temperature perturbations in limb-imaging and lidar observations onboard the research aircraft HALO during the SouthTRAC campaign show remarkable agreement with the IFS data. Ten hours earlier, the IFS data show an "X-shaped" pattern in the temperature perturbations emanating from the sheared tropopause fold. Tendencies of the IFS wind components show that these gravity waves are excited by spontaneous emission adjusting the strongly divergent flow when the PFJ impinges the STJ. In situ observations of temperature and wind components at 100 Hz confirm upward propagation of the probed portion of the gravity waves. They furthermore reveal embedded episodes of light-to-moderate CAT, Kelvin Helmholtz waves, and indications for partial wave reflection. Patches of low Richardson numbers in the IFS data coincide with the CAT observations, suggesting that this event was accessible to turbulence forecasting.

Plain Language Summary Gravity waves play an in important role in vertical and horizontal energy transport in the atmosphere and are significant factors in wheather forecasting and climate projections. Among other processes, tropospheric jet streams are known to be sources of gravity waves. They furthermore can be accompanied by tropopause folds (i.e., local tropopause depressions, where stratospheric air can reach deeply into the troposphere) and turbulence, which is relevant for aviation safety. Using a novel combination of airborne observations and data by a state-of-the-art forecasting system, we analyze gravity waves and turbulence during a merger of tropospheric jet streams above the southern Atlantic. The observations show a high degree of agreement with the forecast data from the troposphere to the stratosphere. Ten hours earlier, the forcast data show an "X-shaped" gravity wave structure that emerges from a highly sheared tropopause fold between the merging jet streams. Fast in situ observations at the flight level provide information on the characteristics of the observed waves and show light-to-moderate turbulence, small-scale waves and indications for partial wave reflection. The observed turbulence events are consistently located in regions where the forecast data suggest potential for turbulence.

Key Points:

- Non-orographic internal gravity waves and clear air turbulence are observed in merging jet streams
- State-of-the art high resolution forecast agrees with novel combination of airborne sensors
- "X-shaped" gravity wave feature resulting from merging jet streams at a highly sheared tropopause fold

Correspondence to:
W. Woiwode,
wolfgang.woiwode@kit.edu

Citation:
Woiwode, W., Dörnbrack, A., Geldenhuys, M., Friedl-Vallon, F., Giez, A., Gulde, T., et al. (2023). Non-orographic gravity waves and turbulence caused by merging jet streams. *Journal of Geophysical Research: Atmospheres*, *128*, e2022JD038097. https://doi.org/10.1029/2022JD038097

Received 28 OCT 2022
Accepted 28 JUN 2023

1. Introduction

Jet streams and fronts are important sources of non-orographic gravity waves. Their complex generation mechanisms are subject of ongoing research (Plougonven & Zhang, 2014). Within limited domains and times,

non-orographic gravity waves have been shown to contribute to the vertical momentum flux in a manner that is comparable to orographic sources (Dörnbrack, Eckermann, et al., 2022; Hertzog et al., 2008; Plougonoven et al., 2013). Different excitation mechanisms, often occurring within geostrophic adjustment processes (e.g., O'Sullivan & Dunkerton, 1995), are reported in literature. They include, amongst other mechanisms, spontaneous emission due to instabilities of the quasi-geostrophic flow, transient generation by sheared disturbances, and shear instabilities on small scale (Plougonven & Zhang, 2014, and references therein). Another relevant mechanism is excitation by the stratospheric flow across propagating Rossby wave trains (Dörnbrack, Eckermann, et al., 2022). Correlation analyses based on intensive radiosonde observations above Wuhan and Yichang, China, have shown that the vertical shear of the horizontal wind at the tropospheric jet is an important source of non-orographic gravity waves in the troposphere and stratosphere (Zhang et al., 2008; Zhang & Yi, 2005, 2007).

Clear air turbulence (CAT) occurs in the vicinity of tropospheric jet streams and represents an important mechanism for mass exchange between the stratosphere and the troposphere (Gettelmann et al., 2011; Shapiro, 1980, and references therein). CAT is of high relevance to global aviation safety (Kennedy & Shapiro, 1975; Sharman et al., 2012, and references therein). Gravity waves generated by jets and fronts can be sources of CAT, since they are accompanied by vertical shear and discontinuities in static stability in the tropopause region (Knox, 1997; Koch et al., 2005; Knox et al., 2008, Plougonven & Zhang, 2016, and references therein). Furthermore, they are able to modify the ambient shear and stability in such a way that instabilities leading to CAT are more easily triggered, a process already mentioned by Panofsky et al. (1968). Thus, it is important to analyze observations of non-orographic gravity waves and CAT associated with tropospheric jet streams and to test whether the associated mechanisms of wave excitation and their effects on conditions supportive to CAT are represented by state-of-the-art forecasting systems.

Non-orographic gravity waves and turbulence in the vicinity of jet streams are difficult to access observationally, since their generation and propagation occurs under non-stationary and transient conditions, often at remote locations (e.g., above oceans) on the globe (Rodriguez Imazio et al., 2022). The standard observational systems that are capable of resolving mesoscale non-orographic gravity waves and, at the same time, the turbulent scale are scarce and observations are mainly limited to selected radiosonde profiles (e.g., Dörnbrack et al., 2018; Plougonven & Teitelbaum, 2003), or to aircraft observations. In the framework of the SouthTRAC mission from September–November 2019, the SouthTRAC-GW (Southern hemisphere Transport, Dynamics, and Chemistry—Gravity Waves) campaign was conducted to probe gravity waves in the hotspot region around the southern part of South America and the Antarctic peninsula (Rapp et al., 2021). Among other objectives, goals of SouthTRAC-GW were to provide detailed measurements of orographic and non-orographic gravity waves for comparisons with high-resolution simulations, to explore breaking and dissipation of gravity waves, and to compare the identification of gravity waves seen by different measurement techniques. During SouthTRAC, the combination of airborne limb-imaging observations below the aircraft by GLORIA (Gimballed Limb Observer for Radiance Imaging of the Atmosphere; Friedl-Vallon et al., 2014; Riese et al., 2014) with ALIMA (Airborne Lidar for Middle Atmosphere research; Rapp et al., 2021) above the aircraft and BAHAMAS (Basic Halo Measurement and Sensor System; Giez et al., 2017, 2019, 2021; Krautstrunk & Giez, 2012) at the flight level was available onboard the German research aircraft HALO (High Altitude and Long Range Research Aircraft) for the first time. These observations allowed focused observations of gravity waves from the troposphere to the mesosphere and on the meso-scale and turbulent scale.

The southern hemisphere stratospheric polar vortex during austral winter is usually stable, that is, less affected by planetary waves than its northern hemispheric counterpart, and it lasts long into spring. However, in September 2019, the rare event of a minor sudden stratospheric warming (SSW) in the southern hemisphere occurred after a poleward shift of the polar night jet stream (Dörnbrack et al., 2020; Lim et al., 2021). The mean Antarctic warming in the midstratosphere during spring 2019 resulted in a new record, with a ∼50% higher polar temperature anomaly at 30 hPa than during the first-ever observed sudden stratospheric warming in the southern hemisphere in 2002. At the same time, the deceleration of the vortex was comparable with this previous unusual winter. In the austral winter 2019, tropospheric weather systems were often affected by blocking of the airflow above the Pacific upstream of the southern Andes. This resulted in a less distinct separation of the polar front jet stream (PFJ) and the subtropical jet stream (STJ) (S. Knobloch, 2022, personal communication) and situations where the PFJ approached the STJ under steep angles in the horizontal domain such as analyzed here.

In this study, we analyze non-orographic gravity waves caused by merging jet streams over the Atlantic Ocean far from the South American landmass. These gravity waves were predicted in advance by the ECMWF (European Centre for Medium-Range Weather Forecasts) Integrated Forecast System (IFS) as they were generated during

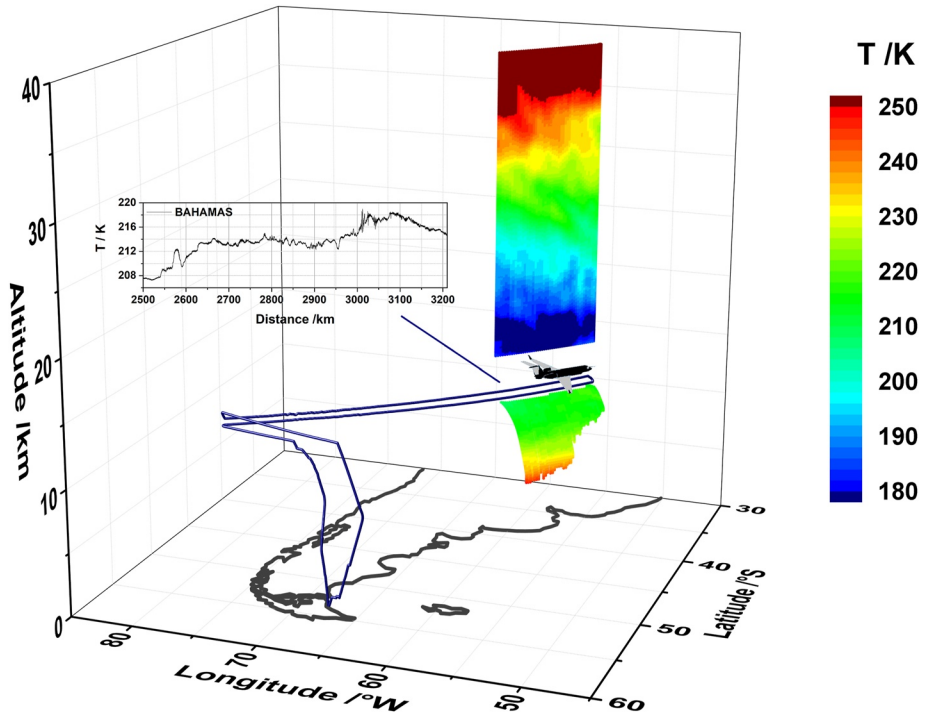

Figure 1. Remote sensing and in situ observations onboard HALO to study gravity waves. Temperature measurements by the GLORIA infrared limb-imager are shown underneath and to the south-east, those from the upward-looking ALIMA lidar are shown directly above the flight track, and BAHAMAS in situ data are displayed schematically in the background for the portion of HALO research flight ST10 examined here.

a merger of the PFJ with the STJ that lead to a strongly deformed horizontal airflow. The scenario is analyzed with the help of ECMWF IFS high-resolution short-term forecasts and operational analyses, as well as dedicated airborne observations by GLORIA, ALIMA and BAHAMAS onboard HALO during the SouthTRAC research flight ST10 on 16–17 September 2019. Thereby, the following research questions are addressed:

- Do the location and the amplitudes of the predicted non-orographic gravity waves in the IFS data agree with the airborne observations? How do the amplitudes agree with those of orographic gravity waves?
- Where is the origin of these gravity waves and how are they excited?
- Are there indications of small-scale waves and CAT, and how are they affected by these non-orographic gravity waves?

In Section 2, the observations, model data and methods used for data analysis are introduced. The overall meteorological situation during ST10 and the jet stream merging event is discussed in Section 3. A detailed analysis of the jet stream merging event and the non-orographic gravity waves based on the IFS data and the observations is presented in Section 4. Using the IFS and trajectories, we investigate the temporal evolution and the origin of the observed waves and turbulence. In Section 5, we discuss our results and conclude the paper.

2. Data and Methods

To study the meteorological situation and non-orographic gravity waves above the southern Atlantic on 16–17 September 2019, we use ECMWF IFS and ERA5 data together with the combination of the instruments GLORIA, ALIMA and BAHAMAS that was deployed onboard HALO during SouthTRAC for the first time (Figure 1).

2.1. GLORIA Limb-Imaging Observations

GLORIA (Gimballed Limb Observer for Radiance Imaging of the Atmosphere) is an infrared limb-imager that has been developed for high-altitude aircraft and stratospheric balloons (Friedl-Vallon et al., 2014; Riese

et al., 2014). In the configuration applied during SouthTRAC, 128 vertical times 48 horizontal pixels of the GLORIA detector array were used for simultaneous limb-imaging observations from ∼5 km up to the flight altitude (typically 12–13 km). Since each pixel records an interferogram, the observations represent data cubes. The interferograms are transformed into spectra, and the spectra associated with one detector row within a data cube are binned, thus resulting in 128 spectra with different limb viewing angles per data cube. The spectral range from 780 to 1,400 cm^{-1} covered by GLORIA includes spectral signatures of many trace gases (e.g., CO_2, O_3, H_2O, chlorofluorocarbons, and pollution gases) and aerosols. The performance and processing of the GLORIA measurements have been improved continuously over the last years. The GLORIA observations during SouthTRAC are characterized by instrumental gain and offset errors as low as 1% and 30 nW cm^{-2} sr^{-1} cm, respectively (Ungermann et al., 2022). From the GLORIA observations, vertical profiles and 3D distributions of temperature, trace gas volume mixing ratios, and clouds are retrieved (e.g., Johansson et al., 2018; Krasauskas et al., 2021; Krisch et al., 2017; Wetzel et al., 2021).

GLORIA can be operated in different measurement modes that include different spectral resolution and sampling. Here, we use GLORIA observations in the "chemistry mode," which involves a high spectral sampling of 0.0625 cm^{-1} in combination with a fixed azimuth orientation (i.e., no tomographic sampling by means of azimuth panning), resulting in one data cube of GLORIA observations and thereby one vertical profile of each target parameter within ∼3 km horizontal flight distance (Johansson et al., 2018). In particular, we use GLORIA temperature (water vapor) profiles, which are characterized by a combined random and systematic error of ∼1 K (∼15%) and a typical vertical resolution of <500 m (<400 m), respectively. The vertical profiles characterize the atmospheric scenario near the tangent points of the GLORIA limb observations, which are located on the right side of the HALO flight track. For each parameter, the individual vertical profiles retrieved from the GLORIA observations are combined to vertical cross-sections along the HALO flight track. Note that the tangent points of the upper limb observations are situated close to the flight level, while they are farther away in horizontal direction for lower viewing angles (see Figure 1). Thus, the vertical cross-sections obtained from GLORIA do not reflect the situation below the flight track (i.e., normal to the earth surface), but are located on a curved surface projected by the GLORIA tangent points along the flight path (see Figure 1). This property is accounted for in the following model comparisons by interpolating the IFS data to the GLORIA tangent points instead of normal to the flight path.

2.2. ALIMA Lidar Observations

ALIMA (Airborne Lidar for Middle Atmosphere research) is an upward pointing Rayleigh lidar which uses an Nd:YAG laser operating at 532 nm wavelength (Rapp et al., 2021). Using three height-cascaded elastic detector channels, atmospheric density profiles from a few kilometers above flight altitude up to 90 km are measured and are converted to temperature profiles by hydrostatic integration in a similar way as with data acquired by ground-based lidar instruments (Kaifler & Kaifler, 2021). For ST10, from 20 to 35 km the corresponding mean absolute error is approximately constant at 1.4 K, since the signal is distributed over the three height-cascaded detector channels, and increases to 5.3 K at 50 km. Below 20 km, absolute errors are larger than 1.4 K. However, relative temperature perturbations induced by gravity waves can still be derived accurately by removing a horizontal mean from the data, thus making the analysis less sensitive to systematic uncertainties (Ehard et al., 2015). The individual ALIMA profiles are combined to form vertical cross-sections above the HALO flight track in the upright direction. Here, we use ALIMA temperature data with 5 min temporal and 1,500 m vertical resolution.

2.3. BAHAMAS In Situ Observations

BAHAMAS is the Basic HALO Measurement and Sensor System (Krautstrunk & Giez, 2012). BAHAMAS consists of a nose boom probe with a 5-hole sensor and provides in situ measurements of horizontal and vertical wind components as well as temperatures, pressures, and water vapor mixing ratios at flight altitude with high temporal resolution, that is, up to 100 Hz (Giez et al., 2017, 2019). Giez et al. (2021) presented a detailed and complete description of the different calibration steps of the BAHAMAS sensor for HALO. Here, we use BAHAMAS measurements of static air temperature and the three wind components u, v, and w. The standard BAHAMAS data products are available with a temporal resolution of 1 and 10 Hz. High temporal 100 Hz resolution can be achieved after a dedicated post processing, which was conducted for the flight section analyzed here. Appendix B of Dörnbrack, Bechtold, and Schumann (2022) contains a comparison of the SouthTRAC

spectra from all available 10 and 100 Hz data. The spectra of the 10 and 100 Hz velocity components are very similar in the 0.4–4 Hz analysis interval applied to determine the energy dissipation rates used in this study, a result that promotes confidence in the well-calibrated BAHAMAS measurements (Giez et al., 2021). According to Krautstrunk and Giez (2012) and Giez et al. (2017, 2019, 2023, and personal communication), the static air temperature data is characterized by absolute errors (1σ) of 0.3 K and the static air pressure data by 0.2 hPa. The absolute errors (1σ) of the horizontal and vertical wind components u, v, and w are 0.3, 0.5, and 0.6 m s^{-1}, respectively.

2.4. ECMWF IFS and ERA5 Data

The IFS is the state-of-the-art global numerical weather prediction system operational at the ECMWF. Here, we use high-resolution 1-hourly deterministic short-term forecasts and six-hourly operational analyses by the IFS (Hólm et al., 2016; Malardel & Wedi, 2016) to analyze the synoptic and mesoscale scenario and its temporal evolution. Note that small discontinuities in the atmosphere variables might result at the transition points from the forecasts to subsequent analyses, which are, however, of minor importance here. The IFS forecast and analysis data are computed on a cubic octahedral grid at a spectral truncation of 1,279, which corresponds to a horizontal resolution of ∼9 km and is interpolated to a regular 0.25° × 0.25° latitude-longitude grid. The data include 137 vertical levels, from the ground up to the model top at ∼0.01 hPa, and have a vertical resolution of ∼400 m in the tropopause region. In particular, we use IFS temperature, pressure, wind, potential vorticity, and specific humidity (q_v) data to investigate the evolution of the atmospheric scenario during SouthTRAC research flight ST10.

For the meteorological flight overview in Section 3, we furthermore show ERA5 data (Hersbach et al., 2020). The data are available at 137 levels from the surface to ∼80 km and provide hourly estimates of atmospheric variables at a slightly coarser horizontal resolution (∼30 km) than the operational IFS products.

2.5. Data Analysis

2.5.1. IFS Fields and Comparison With Observations

We use vertical and horizontal cross sections of the IFS fields to analyze the meteorological situation, gravity waves, and the temporal evolution of the atmospheric variables along the flight track of ST10. For this purpose, the spatially interpolated IFS data are shown at the indicated model time steps without interpolation in time in Figures 3 and 5–8. For the vertical cross sections in these Figures, the IFS data are interpolated to a regular vertical 500 m grid normal to the earth surface and along the main axis of the flight track (see red dashed line in Figure 3a). For comparisons with the BAHAMAS turbulence data in Figure 10, the ECMWF data are also interpolated in time. The squared Brunt–Väisälä frequency

$$N^2 = \frac{g}{\theta}\frac{\partial \theta}{\partial z} \tag{1}$$

and the squared vertical shear of the horizontal wind speed

$$S^2 = \left(\frac{\partial u}{\partial z}\right)^2 + \left(\frac{\partial v}{\partial z}\right)^2 \tag{2}$$

are calculated from the interpolated data. The Richardson number (R_i) is the quotient of N^2 and S^2 (see Mauritsen & Svensson, 2007, and references therein). In the direct comparisons with the remote sensing observations by GLORIA and ALIMA in Figure 4, the IFS data are interpolated linearly in time and space to the measurement geolocations. In case of GLORIA, the interpolation is done along the tangent points (compare Figure 1).

The GLORIA chemistry mode data are characterized by a dense horizontal sampling along flight track (i.e., one profile of all target parameters every ∼3 km) and high vertical resolutions (<500 m), thus providing a resolved picture of the atmospheric scenario *along* flight track. However, data from limb observations without tomographic sampling and corresponding data processing, such as used here, are characterized by a relatively low horizontal resolution along their line of sight (here: across flight track, i.e., along viewing direction). The horizontal resolution is characterized by the width of the weighting function of the radiative transfer. In GLORIA chemistry mode observations, the bulk response is found roughly within ±100 km before and behind the tangent point (Woiwode et al., 2018). Examples of tomographic observations of gravity waves with GLORIA are discussed by for example, Geldenhuys et al. (2023) and Krasauskas et al. (2022). The low horizontal resolution of limb observations

without tomographic sampling and processing can be accounted for by a more complex model interpolation involving observational filters (Ungermann et al., 2011). However, for the comparisons with the GLORIA limb observations shown here, the IFS data are interpolated to the tangent point geolocations of the GLORIA observations without considering an observational filter. This approach is suitable here, since the flight section of research flight ST10 was planned and flown in a way such that strong horizontal gradients of atmospheric variables along the line of sight were avoided. Thus, the dense horizontal sampling *along* flight track was exploited to resolve the atmospheric variations of interest, while the instrument's line of sight was aligned into directions with low variations in the atmospheric quantities.

To account for the limited spacing of the grid on which the IFS data product used here is available (i.e., 0.25° × 0.25°) and interpolation losses, the GLORIA and ALIMA profiles are furthermore subjected each to a moving ∼50 km horizontal mean in the direct comparisons in Figure 4.

2.5.2. Temperature Perturbations by Gravity Waves

To identify temperature perturbations ΔT due to gravity waves in the IFS data, we de-trended the IFS temperature data by subtracting spectrally truncated data with T106 resolution from the fully resolved IFS fields on the same grid. The reader is referred to Sato et al. (2009), Gupta et al. (2021) or Dörnbrack (2021) for similar applications of this method. For direct comparisons with the observations (Figure 4), a different approach was applied for calculating the temperature perturbations for each of the GLORIA, ALIMA and IFS data. In this case, we calculated for each data set the mean temperature profile of the ∼700 km (∼45 min) flight section that is in the focus here. Then, for each data set, the corresponding mean temperature profile was subtracted from the individual temperature profiles along this flight section.

2.5.3. Trajectories

To visualize the timescales and directions of motion of air parcels during the merging process of the two jet streams that induced the excitation of the observed gravity waves, trajectories were calculated with the Hybrid Single-Particle Lagrangian Integrated Trajectory model (HYSPLIT) by NOAA's (National Oceanic and Atmospheric Administration) Air Resources Laboratory (Draxler & Hess, 1998; Stein et al., 2015 and references therein). In particular, we used the HYSPLIT-WEB online tool (https://www.ready.noaa.gov/HYSPLIT.php, last access: 5 July 2022) to calculate backward trajectories based on NOAA's archived Global Forecast System (GFS) 3-hourly forecast data at 0.25° × 0.25° resolution. We mention that isentropic trajectories involve only adiabatic processes and, therefore, do not include detailed mesoscale processes, such as related to cloud formation. However, here we are mainly interested in the large-scale movement of air parcels during the jet stream merging process. Furthermore, the air parcels travel less than 18 hr, so the uncertainties from isentropic trajectories are considered to be acceptable here. Although not identical with the IFS data used in the other analyses, the GFS data are suitable for our purpose, since both model systems are well-proven, involve a similar dynamical core (e.g., Magnusson et al., 2019), and short lead times of less than 1 day are considered.

2.5.4. Turbulence Observations

To quantify the CAT encountered during the flight section analyzed here, the cube root of the energy dissipation rate ε was calculated according to Bramberger et al. (2018, 2020). As discussed by these authors, this parameter is referred to as EDR. For each velocity component u_i ($i = 1,2,3$), $\mathrm{EDR}_i = \varepsilon_i^{1/3}$ whereby the energy dissipation rates are determined by spectral power $S_i(\mathrm{k})$ with the wavenumber k and assuming a $\mathrm{k}^{-5/3}$ law in a frequency range from 0.4 to 4 Hz (Bramberger et al., 2018, 2020; Smalikho, 1997; Strauss et al., 2015). An advantage of using EDR is that it can be calibrated to specific aircraft loads and used to estimate the aircraft response according to the ICAO (International Civil Aviation Organization) categories for "light," "moderate," "severe" and "extreme" CAT (ICAO, 2001; Sharman et al., 2014). Using this approach, EDR values are available for each of the components of the wind vector. Estimates of the energy dissipation rates computed from the 10 Hz as well as 100 Hz BAHAMAS data are available for the whole SouthTRAC research flights, see Dörnbrack, Bechtold, and Schumann (2022). Furthermore, wave energy flux, momentum flux and energy densities are calculated according to Dörnbrack, Bechtold, and Schumann (2022).

3. Meteorological Situation and Flight Overview

The austral winter 2019 was characterized by the earliest observed SSW in the southern hemisphere (Dörnbrack et al., 2020; Lim et al., 2021; Rapp et al., 2021). In August 2019, the center of the stratospheric polar vortex shifted away from the pole and its shape elongated, which was followed by the minor SSW in September 2019.

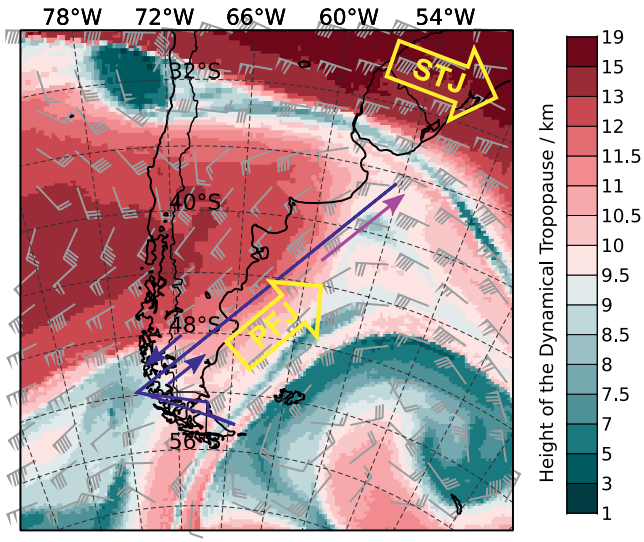

Figure 2. Upper-level atmospheric airflow during the merging event of the polar front jet (PFJ) and the subtropical jet (STJ) valid on 17 September 2019 02 UTC. Height of the −2 PVU surface as a proxy for the dynamical tropopause (km, color-shaded; note the non-linear color scale) and horizontal wind at the dynamical tropopause (short barbs 5 m s^{-1}, long barbs 10 m s^{-1}, triangles 50 m s^{-1}) from ECMWF ERA5 reanalysis. The HALO flight track is indicated schematically by a blue line. Magenta arrow: focus region of this study. Blue arrows: flight directions during the outbound and inbound legs.

A consequence of the displacement was that the cold polar vortex was moved above southern Argentina and Chile. This resulted in the unusual event of mother-of-pearl clouds above El Calafate, Argentina at 50°21′S that were observed visually from ground and the Perlan 2 aircraft (Dörnbrack et al., 2020). In early September 2019, upstream horizontal winds in the upper stratosphere reversed and remained negative or close to zero (Figure 4, Rapp et al., 2021). This generated a critical level for stationary mountain waves (Teixeira, 2014) that confined their vertical propagation to altitudes lower than 40 km for the predominant flow configurations during that period (Rapp et al., 2021). In addition, directional critical levels existed as the wind at upper levels turned significantly from the near-surface wind direction, see Figure 4 in Rapp et al. (2021). At the same time, a blocking anticyclone above the Pacific resulted in weather systems with tropospheric jet streams approaching the southern Andes frequently from western to south-western directions. This resulted in stronger meridional components of the PFJ and thus and a less clear separation of the southern PFJ and STJ when compared to other austral winters. As a consequence, the PFJ approached the STJ under steep angles in the domain analyzed here.

SouthTRAC research flight ST10 was conducted on 16 and 17 September 2019, during the SSW. Figure 2 shows the upper-level airflow by means of the height of the dynamical tropopause and the associated horizontal winds by a synoptic map corresponding to the time of the middle of the flight track. Tropopause maps, as frequently used to visualize and diagnose the upper air flow, have the ultimate advantage to show both tropopause jets in one diagram, see Morgan and Nielsen-Gammon (1998). A strong upper level ridge is seen in Figure 2 above the Pacific, Chile and the northern part of Argentina. A mature upper level trough is located above the Atlantic, east of the Drake Passage with its core north of South Georgia. North of 36°S, a strong STJ is seen that is accompanied by an elongated tropopause fold south of it. Note the bluish-grayish band along the wind maximum of the STJ that indicates tropopause levels between ∼5 and 9 km. The wind in the PFJ is southwesterly across northern Patagonia and above the Atlantic between the upper-level ridge and trough that are located in the north-west and south-east, respectively. In the focus region of this study (magenta arrow in Figure 2), the PFJ has a strong cyclonic curvature and merges with the STJ over the Atlantic. A narrow dip in the tropopause height indicating stratospheric air intruding to lower levels is discernible as a weak bluish spot at ∼39°S/55°W.

The flight track of HALO is plotted schematically in Figure 2. HALO took off in Rio Grande at Tierra del Fuego on 16 September 2019 at 23:00 UTC and crossed the Southern Andes toward the Pacific. After a turn to the north-east, the Andes were crossed again, and HALO flew a long leg across Patagonia and the Atlantic with a north-easterly heading. The outermost waypoint at 36.8°S/54.1°W was reached on 17 September 2019 at 02:40 UTC. Here, HALO turned around and followed the same flight path back to Rio Grande, where it landed at 07:44 UTC.

4. Results

4.1. Synoptic Situation and Gravity Waves in IFS Data

Figures 3a and 3b show the horizontal wind field approximately at flight altitude and along the vertical cross-section of the flight path which is indicated in Figure 3a. Similar to the upper-level airflow shown in Figure 2, the STJ is located in the north-east of the panel, and the PFJ extends from the southern Andes and Patagonia toward the Atlantic, where it merges with the STJ (Figure 3a). In the vertical cross section, the STJ and PFJ are situated at the dynamical tropopause. Here, the polar night jet (PNJ) at about 35 km altitude is located between about 50°W and 65°W which corresponds to low geographic latitudes of about 40°S due to the equatorward shift of the stratospheric polar vortex during the SSW.

At the STJ, a distorted tropopause fold with stratospheric air intruding into the troposphere is seen in Figure 3b. West of the tropopause fold the weak intrusion is seen in the vertical cross section (57°W, compare Figure 2), which was reached by HALO in the outermost section of the flight ("focus region," blue box). While the STJ and

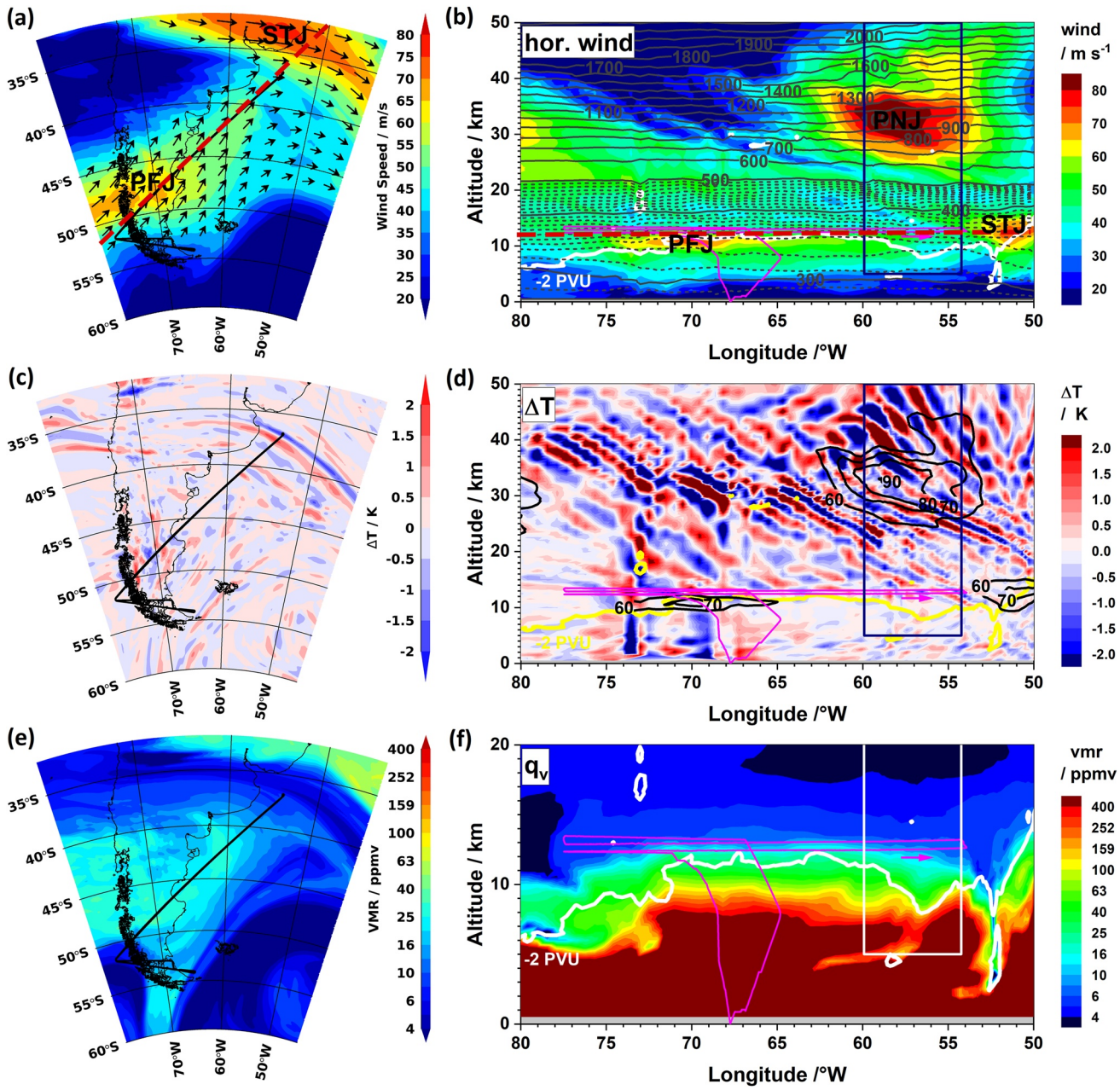

Figure 3. Horizontal (at 200 hPa or ∼12 km altitude) and vertical cross sections of the ECMWF IFS data on 17 September 2019 02 UTC. Horizontal wind speed (a, b) and direction (arrows in a), temperature perturbation (ΔT between $T_{Co}1279$ and T106 resolution data) (c, d), and specific humidity (e, f). Isolines of potential temperature are superimposed in gray in panel (b) (solid gray lines: $\Delta\Theta = 100$ K, dashed gray lines: $\Delta\Theta = 10$ K). The −2 PVU isoline is indicated by white/yellow lines in the vertical cross sections. Selected isolines of horizontal wind (black solid lines, in m s^{-1}) are overlaid in panel (d). The flight track is indicated by black/magenta solid lines in the horizontal/vertical cross sections. Red dashed lines in panels (a, b) indicate the intersection between the horizontal and vertical cross sections shown in the left and right column, respectively. Black arrows in panel (a) indicate the horizontal wind direction and speed at wind speeds ≥40 m/s. Blue and white boxes in (b, d) and (f), respectively, highlight the "focus region" (see text). PFJ = polar front jet, STJ = subtropical jet, PNJ = polar night jet.

PFJ reach maximum wind speeds larger than 70 m/s in their core regions, moderate wind speeds of around 50 m/s are found in their merging zone. Within and around the focus region, slanted patches of lower wind speeds less than 40 m/s are found above the tropopause indicating layers of enhanced horizontal wind shear. They coincide with regions where a steepening of isentropic surfaces is seen between the tropopause and the PNJ in Figure 3b.

Figures 3c and 3d show the IFS temperature perturbations ΔT due to gravity waves, calculated using the method described in Section 2.5.2. In the horizontal cross section (Figure 3c), elongated, bow-shaped phase lines with

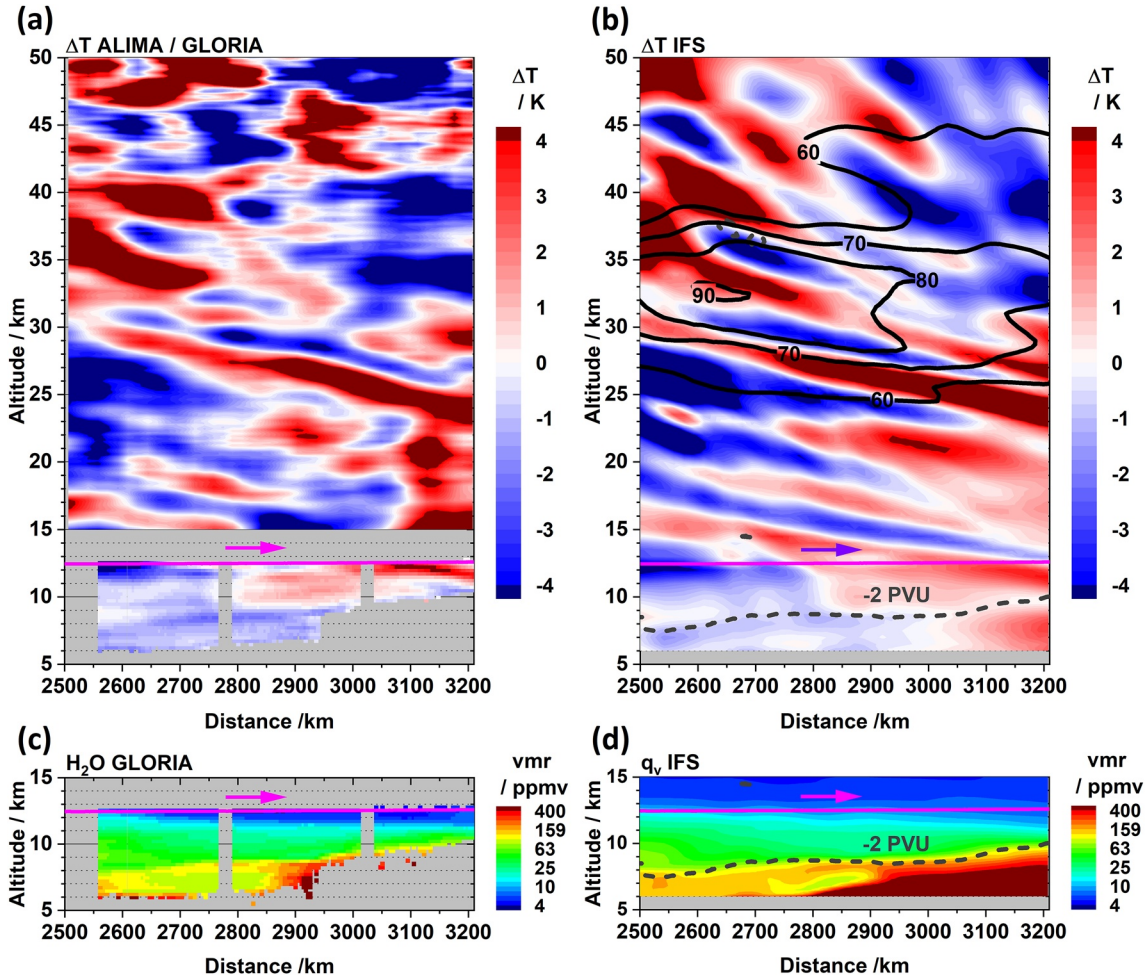

Figure 4. Observed and forecasted temperature perturbations. (a) Temperature perturbation calculated from ALIMA (above 15 km) and GLORIA (below 12.5 km). (b) Temperature perturbation calculated from IFS data. (c) GLORIA water vapor and (d) IFS specific humidity for the same flight section. For details of the comparison, see Sections 2.5.1 and 2.5.2. HALO flight altitude (magenta solid line, all panels), selected isolines of horizontal wind speed (black solid lines in (b), in m s^{-1}), and dynamical tropopause (dashed dark gray lines in (b, d)).

moderate maximum values of $\Delta T = \pm 2$ K are situated along the STJ and are touched by the outermost part of the research flight ST10. In the vertical cross section (Figure 3d), these phase lines reach from the upper edge of the poleward side of the tropopause fold diagonally into the lower stratosphere. At about 20 km, these phase lines interfere and combine with other phase lines with larger amplitudes in ΔT. Most probably, these gravity waves are from different sources that are not connected with the sheared region in the tropopause fold. Further phase lines with relatively high ΔT at stratospheric altitudes between 66° and 74°W are probably the consequence of mountain waves above the southern Andes. The seemingly vertically aligned patterns below are interpreted to result from the different representation of the cross-mountain flow at the two model resolutions. Note that clear wave signals can only be expected in the stratosphere due to the absence of other mesoscale processes having higher wavenumbers than 106 (compare Section 2.5.2). In contrast, intense synoptic tropospheric systems or the pressure distribution of the airflow across mountains can produce spurious phase lines in the troposphere that are not indicative of propagating gravity waves. At altitudes higher than 20 km, mountain waves between 66° and 74°W interfere and combine with other phase lines to a complex entity. The sources of this gravity wave mix are probably the horizontal propagation of orographic waves, secondary waves, and/or non-orographic gravity waves near the PFJ, PNJ, and STJ. However, the non-orographic gravity waves at the tropopause fold that were probed by ST10 are assumed to be largely unaffected by these gravity waves from other sources.

The distribution of specific humidity is shown in Figures 3e and 3f. In Figure 3e, higher water vapor mixing ratios in the lower stratosphere at ∼12 km between about 38° and 50°S above the Pacific, Andes and Patagonia

are related to the upper level ridge seen in Figure 2. Dry air masses in the south-east are due to the fact that the 200 hPa surface is here in the stratosphere above the upper level trough. In the north-east, high specific humidity indicates the step in the tropopause at the STJ. An elongated dry band from ∼35°S in the west to ∼40°S in the east corresponds to the tropopause fold seen in Figure 2. In the vertical cross section in Figure 3f, the steep increase from low and approximately constant stratospheric water vapor mixing ratios toward tropospheric values begins mostly a few kilometres above the tropopause. Around the tropopause, variable water vapor mixing ratios of the order of 10 to 50 ppmv and strong vertical gradients of specific humidity are found (greenish colored region in Figure 3f). In the vicinity of the tropopause fold between 51° and 55°W, dry air masses reach down to altitudes lower than 3 km. In the intrusion left of it, moist air masses remain high whilst the dynamical tropopause is lowered. A comparatively dry band stretches from the intrusion down to ∼5 km altitude and then horizontally to the south-west.

In summary, the phase lines probed in the focus region of the flight ST10 reach from the upper edge of the poleward side of a tropopause fold into the lower stratosphere. They are situated in a region affected by horizontal wind shear between the PFJ and STJ and above an intrusion of stratospheric air into the tropopause.

4.2. Comparison of IFS With GLORIA and ALIMA

A remarkable agreement is found for the comparison of the temperature perturbations extracted from the GLORIA and ALIMA (Figure 4a) data with ones from the IFS data (Figure 4b). As discussed in Section 2.5.2, a different approach than in Figures 3c, 3d, 5 and 8a is applied here for extracting temperature perturbations by gravity waves to enable a direct comparison of the different data sets. Naturally, a one-to-one correspondence between the observations and the forecast/analysis data cannot be expected. Nevertheless, all major phase line patterns below 40 km simulated by the IFS correspond to phase lines in the airborne remote-sensing observations in the troposphere as well as stratosphere: In particular, (a) the cold anomaly around flight altitude before the distance of 2,800 km, (b) the warm phase line stretching from an altitude of ∼16 km altitude at 2,500 km downwards to ∼11 km altitude at 3,200 km, (c) and another large warm phase line at higher altitudes, reaching from ∼30 km altitude at 2,500 km downwards to ∼24 km altitude at 3,200 km. Further corresponding warm and cold anomalies ΔT are found in the model data and observations at all altitudes. The amplitudes of the temperature perturbations ΔT compare well between the IFS data and observations. Slightly lower maximum amplitudes in the IFS data, mainly below 25 km, can be explained by the limited model resolution. Note that the major phase lines in the IFS data are aligned in an almost identical orientation compared with the airborne observations. A lower degree of agreement of the amplitudes of ΔT above 40 km is probably related to increased layer level spacing and artificial damping in the IFS model (e.g., Gisinger et al., 2022).

Along the dynamical tropopause, a weak ΔT minimum is found consistently in both the observations and model data (see bluish to white contours around −2 PVU isoline in Figure 4b and similar pattern in Figure 4a). Missing data points in the GLORIA data before ∼2,550 km and, below the tropopause beyond a distance of 2,950 km, are due to a change in the GLORIA measurement mode and opaque tropospheric clouds, respectively. Note that the shape of the dynamical tropopause appears different here when compared with Figure 3, since the IFS data are interpolated here at the measurement times and, below flight level, along the geolocations of the tangent points of the GLORIA observations (see horizontal displacement of GLORIA tangent points from flight path in Figure 1).

A satisfying agreement is also found between the structures seen in GLORIA water vapor and IFS specific humidity (Figures 4c and 4d). The transition from moist tropospheric to dry stratospheric water vapor mixing ratios in the intrusion seen in the observations is consistently reproduced by the model. A dry filamentary structure below the tropopause prior to a distance of 2,900 km agrees at least qualitatively in the two data sets. Consistent with other studies (e.g., Bland et al., 2021; Dyroff et al., 2015; Stenke et al., 2008; Woiwode et al., 2020) a systematic moist bias is found in the model data in the entire region. However, the comparison confirms that the tropopause, the structure of the intrusion, and the absolute mixing ratios are simulated by the IFS in a realistic way.

4.3. Evolution of Non-Orographic Gravity Waves

In Figures 5 and 6, various diagnostics display the temporal evolution of the simulated non-orographic gravity waves and the jet stream merging event during central part of the flight at 02 UTC on 17 September 2019

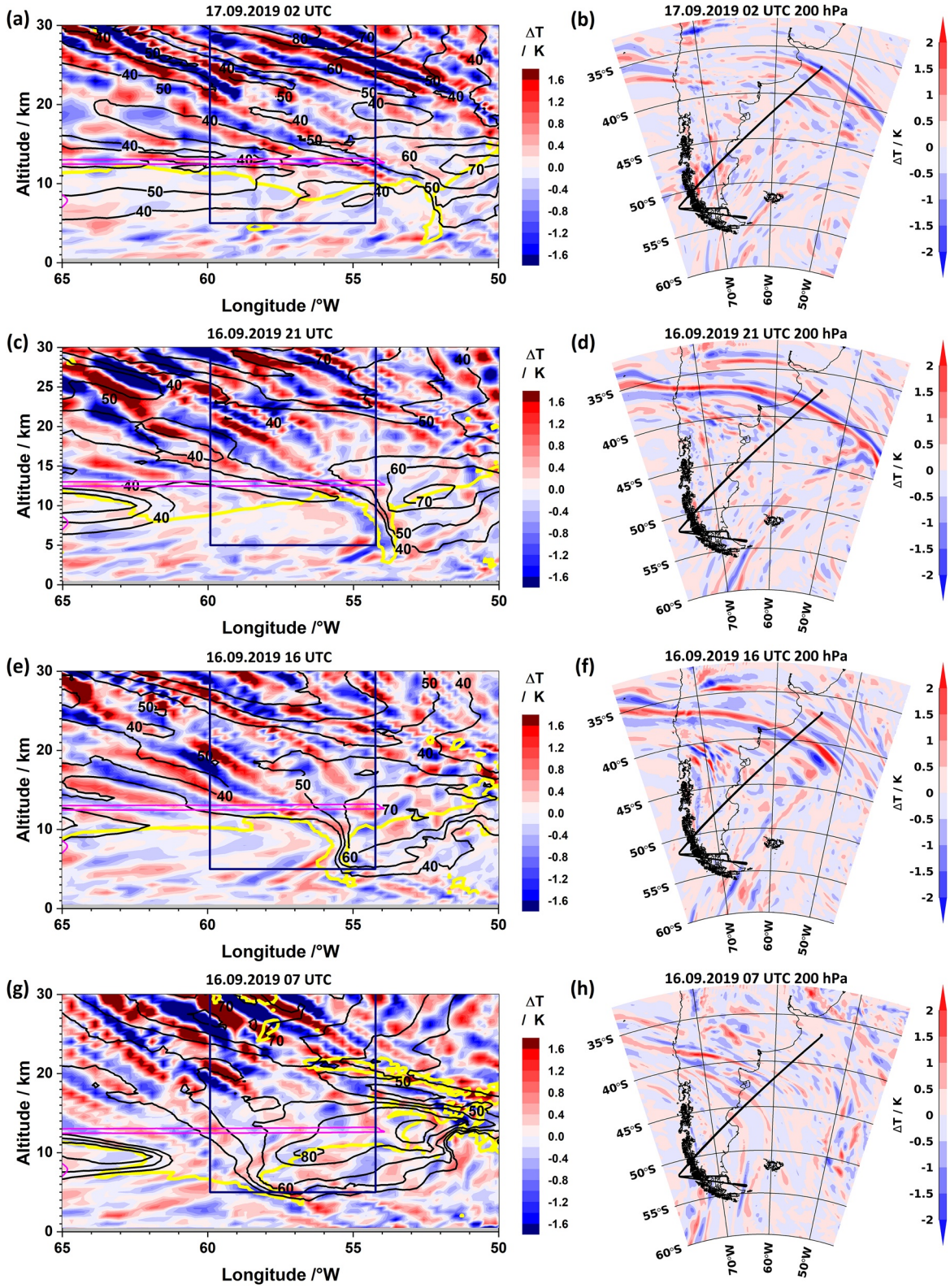

Figure 5. Evolution of non-orographic gravity waves during jet stream merging event in IFS data at central time of the flight (1st row) and 5 hr (2nd row), 10 hr (3rd row), and 19 hr (4th row) before. (a, c, e, g) Vertical distributions of temperature perturbation along main axis of flight from 50° to 65°W. (b, d, f, h) Temperature perturbation at 200 hPa (~12 km altitude). Selected isolines of horizontal wind (black solid lines, in m s^{-1}) and the −2 PVU isoline (yellow solid line) are overlaid in the vertical cross sections. The flight track is indicated by magenta/black solid lines in the vertical/horizontal cross sections.

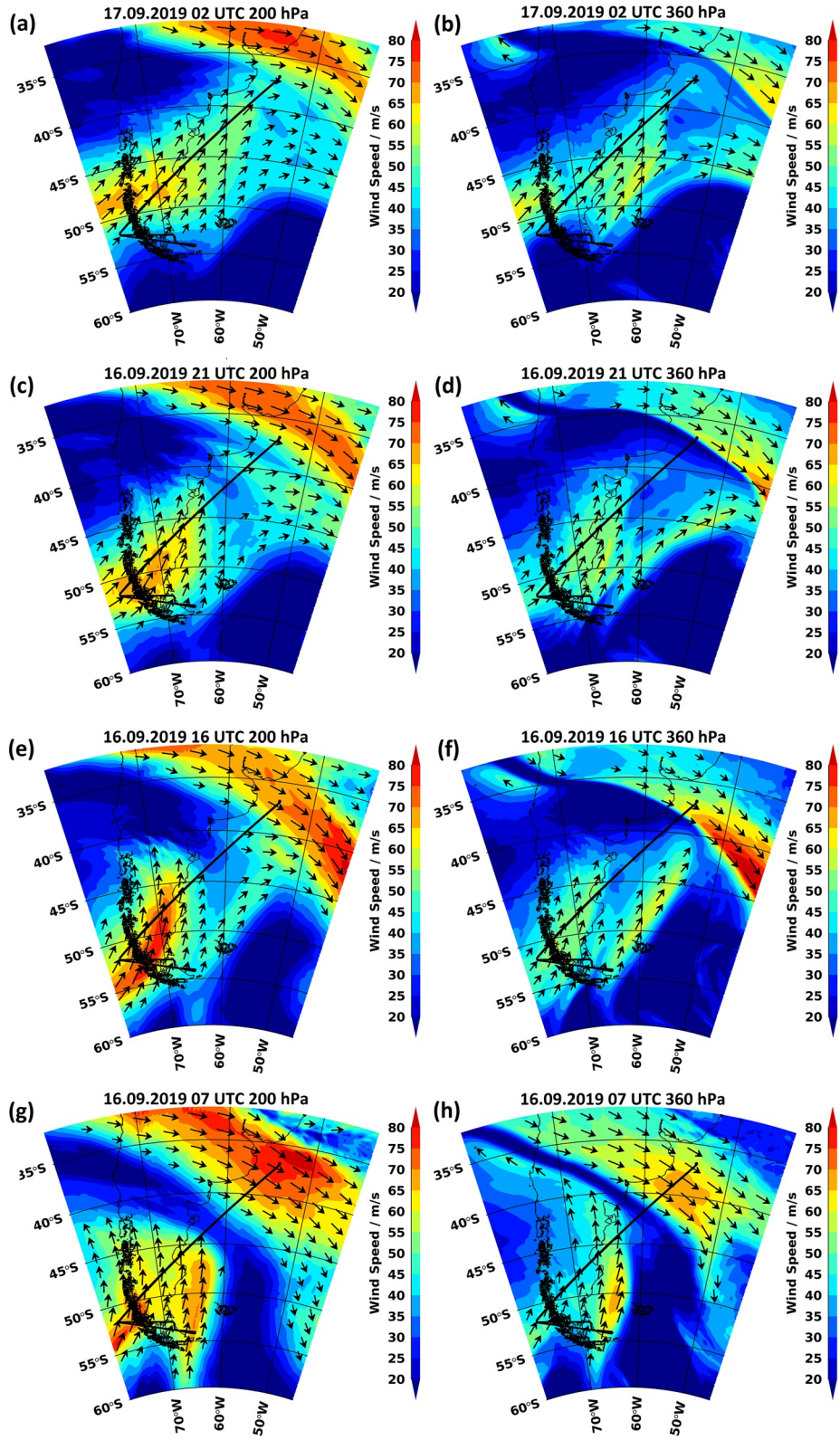

Figure 6. Evolution of horizontal wind field during jet stream merging event in IFS data at central time of the flight (1st row) and 5 hr (2nd row), 10 hr (3rd row), and 19 hr (4th row) before. Horizontal wind speed and direction (a, c, e, g) at 200 hPa (~12 km altitude) and (b, d, f, h) at 360 hPa (~8 km). Black arrows indicate the horizontal wind direction and speed at wind speeds ≥40 m/s. The flight track is indicated by black solid lines.

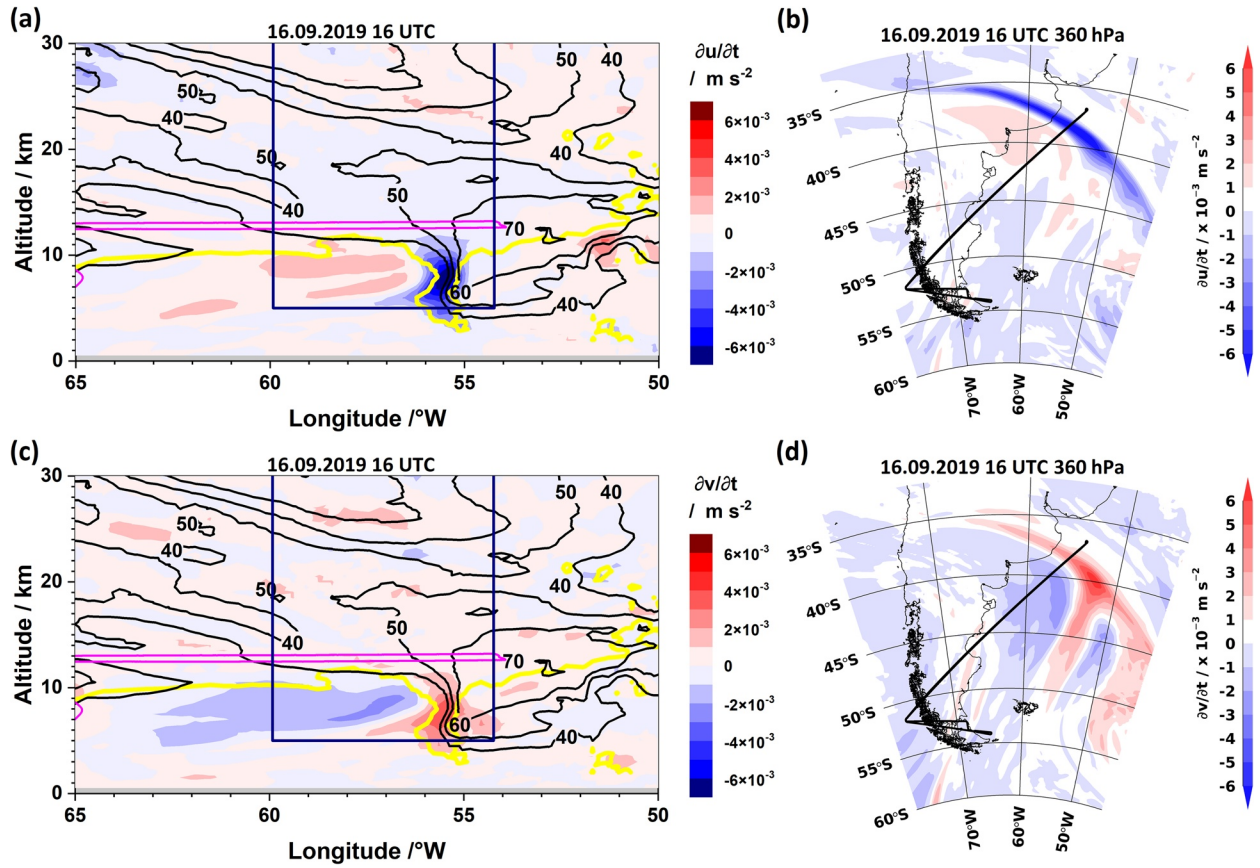

Figure 7. Tendencies in the horizontal wind components 10 hr before the central time of the flight. The vertical and horizontal (at 360 hPa or ∼8 km altitude) cross sections show the de-/acceleration of the (a, b) zonal and (c, d) meridional wind components. Selected isolines of horizontal wind speed (black solid lines, im m s^{-1}) and the −2 PVU isoline (yellow solid lines) are overlaid in panels a and c. The flight track is indicated by magenta/black solid lines in the vertical/horizontal cross sections.

(1st rows) and 5 hr (2nd rows), 10 hr (3rd rows) and 19 hr (4th rows) before. In order to follow the actual temporal sequence of the event, one has to read Figures 5 and 6 from bottom to top. The horizontal wind field is shown in Figure 6 at a level of ∼12 km, which was the flight altitude during the in situ observations, and ∼8 km, where the source region of the non-orographic gravity waves is situated (see Figures 7a–7d and 8a).

At the time HALO flew through the flight segment we are focusing on (the central time of the flight), phase lines with moderate amplitudes ΔT extend from the upper edge of the poleward side of the tropopause fold into the lower stratosphere and cross the flight path as shown in Figure 5a. At this time, the merging of the jet streams is in full progress. In the western half of the plot the PFJ is almost perpendicular to the STJ and in the eastern half the PFJ has aligned approximately parallel to the STJ both at flight level and in the upper troposphere (compare Figure 5a with Figures 6a and 6b).

Phase lines with notably larger ΔT at the tropopause fold (Figure 5c) and at flight level (Figure 5d) are found 5 hr earlier. At this time, upward and pronounced downward pointing phase lines extend from the shear region in the tropopause fold into the lower stratosphere and the troposphere, respectively (Figure 5c). In the lowermost stratosphere, these phase lines stretch horizontally across more than 3,000 km in west-east direction along the STJ (Figure 5d). In the eastern part of Figure 5d, southwest-northeast oriented phase lines are connected with this bow-shaped gravity wave pattern. They seem to be related to the cyclonically curved PFJ over the Atlantic Ocean (Figure 6c). At this time, the main part of the PFJ is aligned approximately perpendicular to the STJ in the lowermost stratosphere (Figure 6c) and troposphere (Figure 6d), while a smaller pronounced jet streak at the eastern part of the PFJ aligns already with the STJ.

Ten hours before the central time of the flight (Figure 5e) and west of ∼55.3°W, a sequence of 3 warm and 2 cold interleaved upward- and downward pointing phase fronts can be clearly identified and stretch from the shear region in the tropopause fold in south-westward direction into the lower stratosphere and the troposphere. The same sequence of phase fronts is identified in the horizontal cross section in the lowermost stratosphere (Figure 5f). A weaker, but clearly discernible pattern is found in the vertical domain in opposite direction (Figure 5e), thus forming an "X-shaped" structure centered at ∼55.3°W and an altitude of ∼8 km. Also here, corresponding phase lines are seen in the horizontal domain in Figure 5f. At the same time, the PFJ is oriented in a south to south-west direction above Patagonia (Figures 6e and 6f). The smaller streak at the eastern side of the PFJ produces a confined local horizontal wind maximum that encounters the STJ approximately perpendicularly.

Weak, but still discernible temperature perturbation ΔT in form of coherent phase lines are found 19 hr before the central time of the flight (Figures 5g and 5h). We show this particular time step to document the "initial" situation, since the bow-shaped phase lines become notably more pronounced in the subsequent time steps. Note the opposite orientation of the PFJ with respect to the STJ in the lowermost stratosphere and upper troposphere over Argentina and the Pacific Ocean (Figures 6g and 6h). At 360 hPa, these jets are oriented fully antiparallel. In between, a narrow band of low wind speeds and strong horizontal wind shear is forecasted by the IFS. The jet streak in the east as seen in the previous panels is more developed here and joins from the south with the PFJ.

A full change of the PFJ direction from approximately antiparallel to parallel with respect to the STJ and the temporal evolution of a strongly sheared tropopause fold are documented in Figure 6 when read from bottom to top. Note the turning of the horizontal wind at ∼8 km as the PFJ changes its direction when reading panels 6h, 6f, 6d, and 6b as a sequence. Gravity waves are excited along the strongly diverging flow where the PFJ impinges and merges with the STJ. As a result, gravity wave-induced temperature perturbations ΔT appear along the sheared tropopause fold over more than 3,000 km in horizontal direction. The vertical sections in Figure 5 reveal that these waves are able to propagate from the tropopause level both upward into the stratosphere and downward into the troposphere.

A developed X-shaped pattern with moderate amplitudes in ΔT is found 10 hr before the central time of the flight (Figure 6e). To analyze the specific forces that accompany the excitation of these gravity waves, we investigate the acceleration and deceleration of the horizontal wind components u and v at this time in Figure 7. A strong deceleration ($\geq -7{\cdot}10^{-3}$ m s^{-2}) of the zonal wind and a strong acceleration ($\leq 4{\cdot}10^{-3}$ m s^{-2}) of the meridional wind are found in a small region within the tropopause fold as shown in Figures 7a and 7c. This is exactly at the location where the PFJ impinges the STJ (compare Figure 6f) and where the X-shaped pattern is centered. In the horizontal domain (Figures 7b and 7d), it is seen that the zonal deceleration and meridional acceleration occurs along the sheared bow-shaped band along the STJ as the PFJ impinges the STJ and reverses its direction (compare Figure 6f). The deceleration and acceleration, respectively, are highest in the area where the jet streak along the PFJ "pushes" against the STJ.

Figure 8a shows a zoom into the X-shaped pattern of the phase lines. To visualize the timescales and directions of the large scale motion of air parcels during the merging of the two jet streams, isentropic backward trajectories are calculated with HYSPLIT to derive the paths of the different air masses interacting with each other in the tropopause fold 10 hr before the central time of the flight. In Figure 8b, the starting points of one trajectory at the poleward (blue) and one trajectory at the equatorward (red) side of the tropopause fold are marked. The starting points are located at 56° and 55°W at an altitude of 8 km in the central region of the X-shaped pattern of the phase lines shown in Figure 8a. In Figure 8c, the backward trajectory starting at the equatorward side of the tropopause fold follows the STJ, while the trajectory starting from the poleward side follows the PFJ as it approaches the STJ. Figure 8d highlights the position of the backward trajectories in the horizontal wind field 9 hr before the starting point (compare Figure 6, 4th row). Here, the location of the backward trajectory from the poleward side coincides with the edge of the maximum in wind speed of the jet streak along the PFJ as it approaches the STJ.

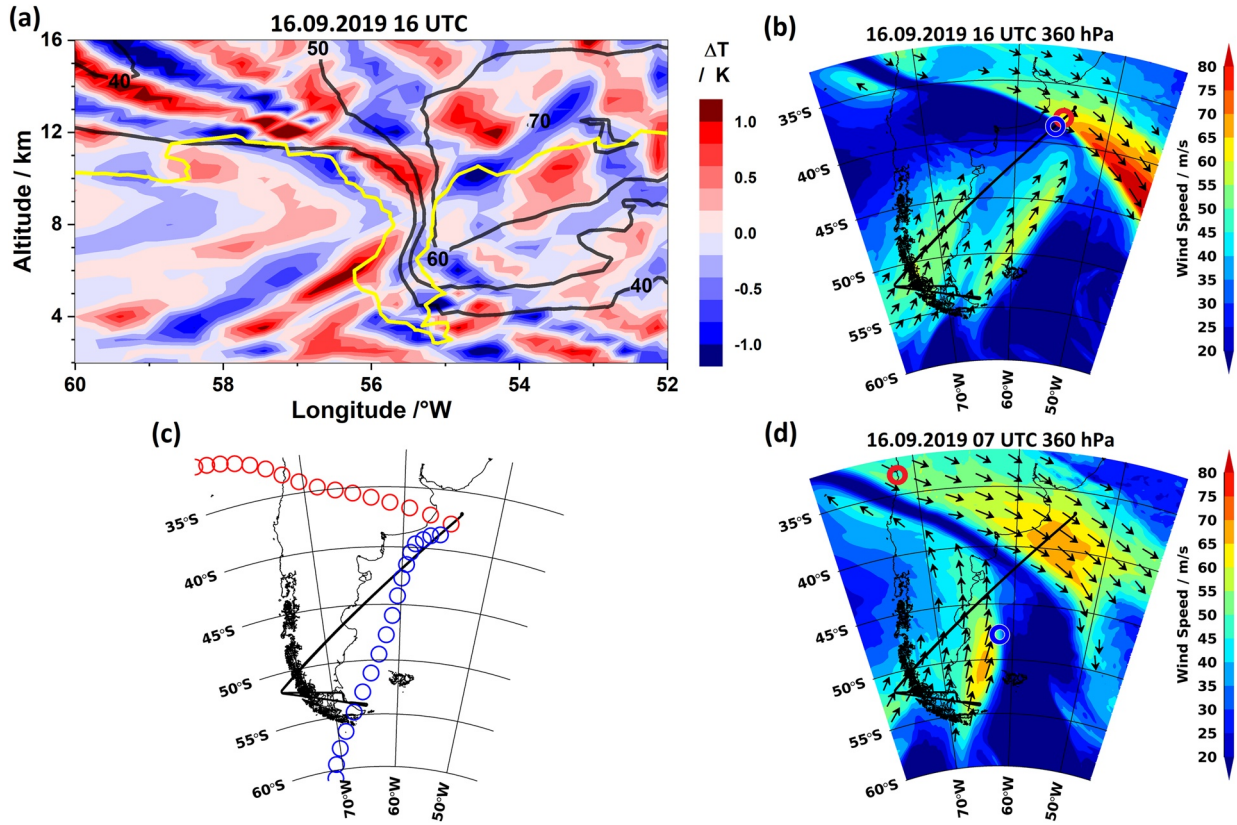

Figure 8. Zoom into "X-shaped" phase line pattern 10 hr before the central time of the flight and HYSPLIT isentropic backward trajectories starting in the center region of the structure. (a) Vertical distribution of temperature perturbation along main axis of flight from 60° to 52°W together with isolines of horizontal wind (black solid lines, in m s^{-1}) and −2 PVU isoline (yellow solid line). (b) Horizontal wind speed and direction at 360 hPa (~8 km altitude) at starting time of trajectories. (c) Geolocations of trajectories (spacing between circles: 1 hr, time range: ≥17 hr). (d) Horizontal wind speed and direction at 360 hPa (~8 km altitude) at 9 hr before trajectory starting point. Black arrows in panels (b, d) indicate the horizontal wind direction and speed at wind speeds ≥40 m/s. The flight track is indicated by black solid lines in the horizontal cross sections.

4.4. Embedded Small-Scale Gravity Waves and Turbulence

The BAHAMAS in situ observations provide a highly resolved view at the temperature and the wind components at flight level and down to scales relevant for turbulence (Figure 9). In the considered flight section, the temperature increases by about 10 K toward the northeast before it falls slightly in the vicinity of the northernmost waypoint (Figure 9a). GLORIA (magenta circles) and BAHAMAS (black line) temperatures are in excellent agreement beyond a distance of 2,800 km. Prior to 2,800 km, slight differences between BAHAMAS and GLORIA can be explained by local temperature variations which are seen differently by the two measurement techniques (i.e., BAHAMAS exactly at flight track and GLORIA in limb geometry to the right hand side). A horizontal wavelength along the flight direction of roughly 300 km is estimated for the non-orographic gravity wave from the BAHAMAS and GLORIA temperature data. Due to the higher temporal and spatial resolution, BAHAMAS resolves much more small-scale fluctuations in the temperature distribution than the GLORIA remote sensing observations. The overall variation of the zonal and meridional wind components and lots of fine structures are seen in the BAHAMAS data in Figures 9c and 9e. In the vertical wind, the BAHAMAS data show considerable high-frequency variations down to the sub-kilometer scale and peak values exceeding ±4 m/s in a short 25 km long interval starting at a distance of 3,000 km (Figure 9g).

A zoom into this region with the strongest variations in vertical wind is shown in the right column of Figure 9. An oscillation is seen in the temperature data with a horizontal wavelength of ~2 km and a maximum peak-to-peak amplitude of 4 K (Figure 9b). Further fine structures well below horizontal scales of 100 m are superimposed. Note, due to the high-resolution 100 Hz data, the spatial resolution of the BAHAMAS observations is about 2.5 m in the horizontal. Complex structures with a similar periodicity and further fine structures are found also in the horizontal wind components (Figures 9d and 9f). A developed oscillation in the vertical wind component

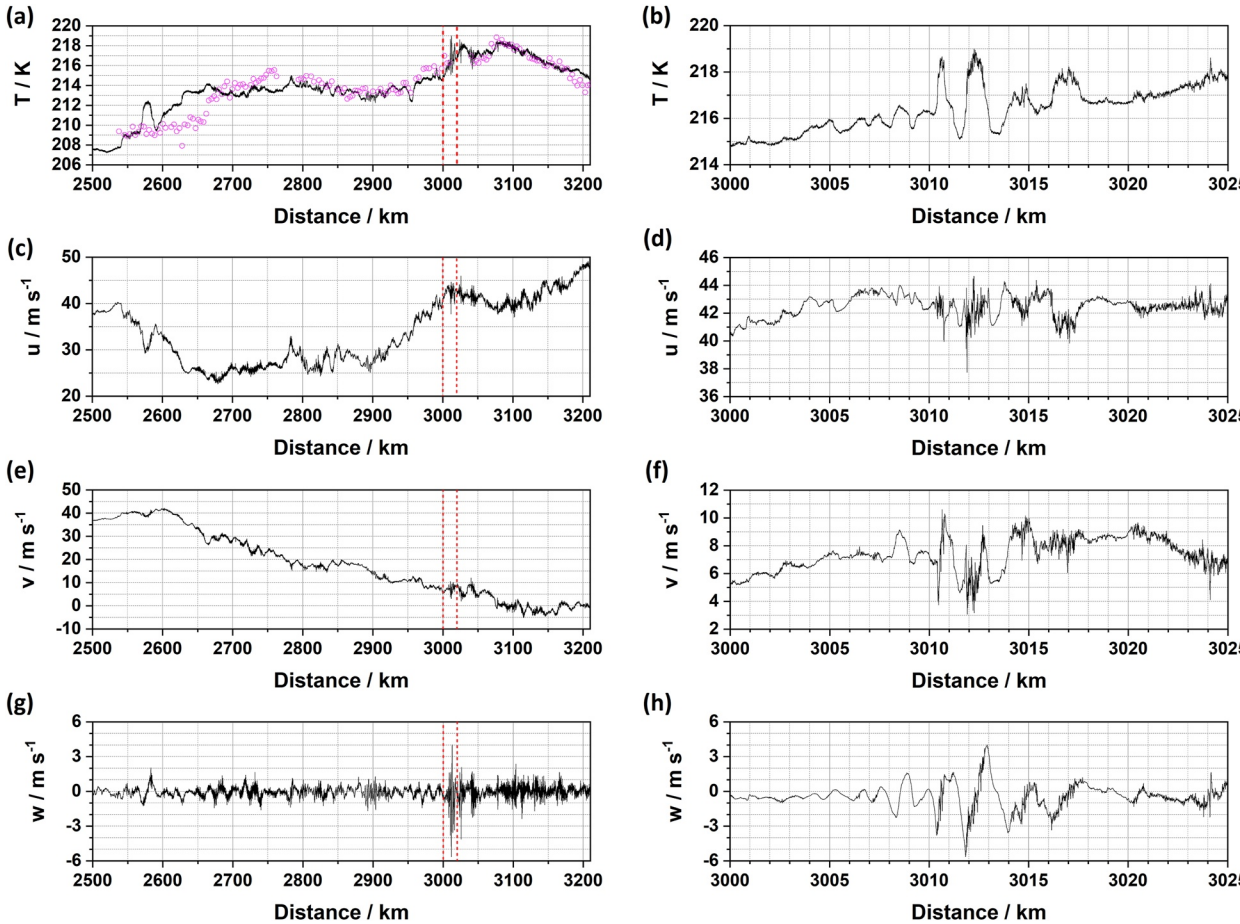

Figure 9. BAHAMAS in situ observations of meteorological variables during flight section in focus (left column) and zoom at location of Kelvin-Helmholtz wave (right column). Black solid lines indicate (a, b) temperature, (c, d) zonal wind, (e, f) meridional wind, and (g, h) vertical wind. GLORIA observations are shown in panel (a) in magenta. Red dashed lines in the left columns mark the section shown in the right column.

(Figure 9h) with a horizontal wavelength of ∼2 km and a phase shift of $\pi/2$ with respect to the oscillation seen in the temperature data (Figure 9b) indicates that a Kelvin-Helmholtz wave (compare e.g., Browing et al., 1970; Chilson et al., 1997) is seen here. Notable variations on turbulent scales are superimposed on the Kelvin-Helmholtz wave and in its vicinity and indicate that turbulent processes are in progress here.

To investigate the situation of the Kelvin-Helmholtz wave and turbulence, the squared Brunt–Väisälä frequency (N^2), the squared shear parameter (S^2) and the Richardson number (R_i) calculated from the IFS data are shown around flight altitude in Figure 10. These quantities are shown together with the cube root of the energy dissipation rates (EDR) calculated from the BAHAMAS data, see Dörnbrack, Bechtold, and Schumann (2022). The N^2 distribution (Figure 10a) shows tilted bands of enhanced and decreased static stability due to the modulation by the non-orographic gravity waves (compare Figures 4a and 4b). A similarly tilted pattern is also found in the distribution of S^2 (Figure 10b). The combination of the modulated static stability and the regions of locally enhanced wind shear results in patches of R_i values lower than ∼3 (Figure 10c). Typically, R_i values less than 0.25 indicate turbulence generation. However, R_i values calculated from model data rarely show such low values due to limited model resolution and interpolation losses. Hence, the minimum of the R_i values are compared qualitatively with EDR. These patches intersect with the flight altitude between 2,550 and 2,850 km, and between 2,950 and 3,200 km, and coincide well with episodes where EDR values calculated from the BAHAMAS data for the three wind components approach and exceed 0.05 $m^{2/3}$ s^{-1} and locally reach maximum values of 0.10 to 0.15 $m^{2/3}$ s^{-1} (Figure 10d). According to Bramberger et al. (2018, 2020), such values are indicative of light to moderate CAT for a HALO-size aircraft. In summary, the combination of the static stability, modulated by the non-orographic gravity waves, and locally enchanted shear formed localized regions with small values of R_i,

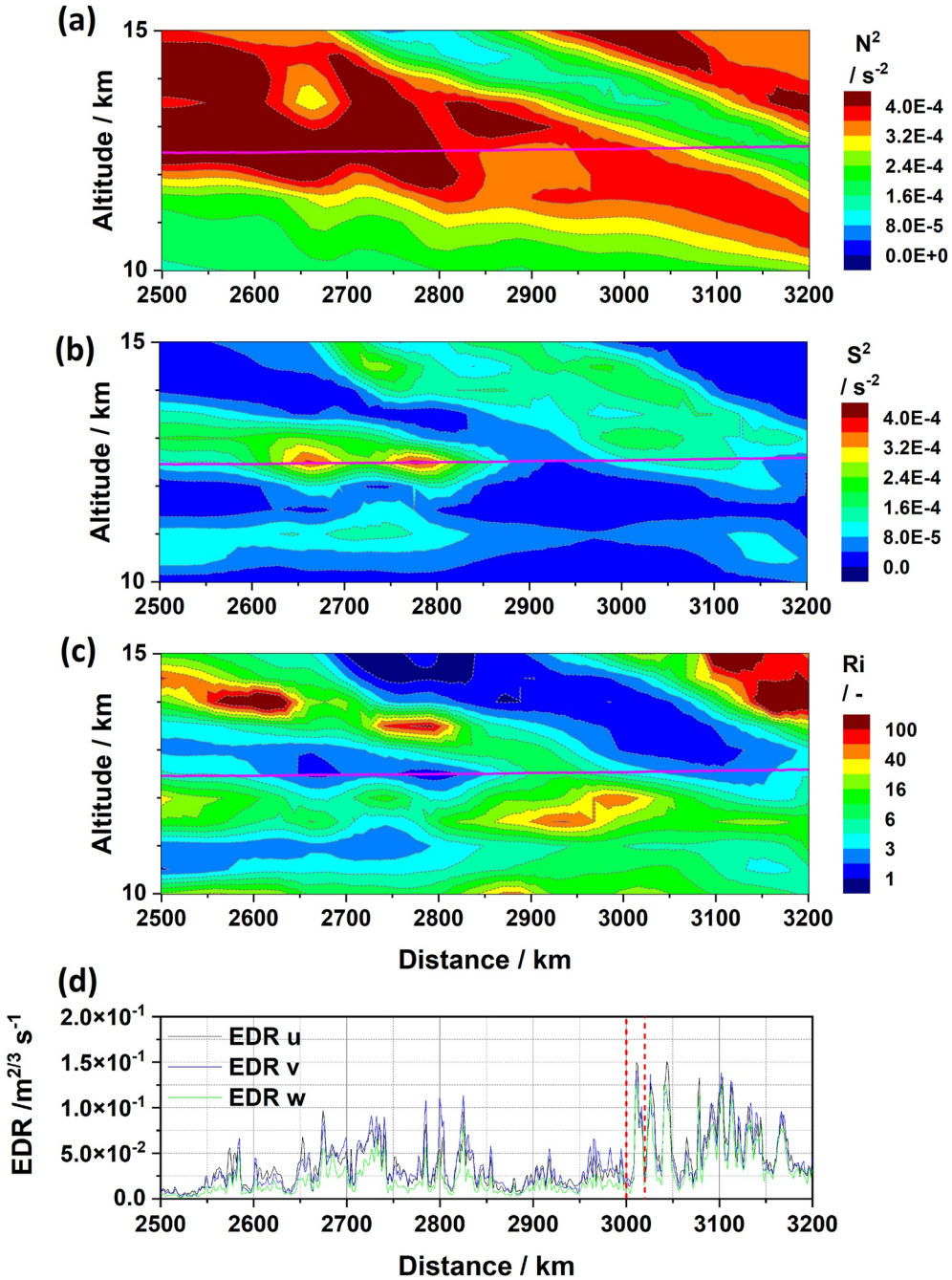

Figure 10. Comparison of (a) squared Brunt–Väisälä frequency (N^2), (b) squared shear parameter (S^2) and (c) Richardson number (R_i) calculated from the IFS data around flight level. (d) EDR calculated from the 100 Hz BAHAMAS data for the three wind components. Note, "*u*" and "*v*" refer to the forward and sideward direction with respect to the flight path in this context. The flight altitude is indicated by magenta solid lines in (a, b, c).

where flow instabilities can grow rapidly. Overall, this burst of turbulence was not a truly severe event, most likely due to the long horizontal wavelength that causes the change in stratospheric airflow.

Overall, the BAHAMAS data show good agreement with GLORIA on mesoscale, but resolve much more fine structures for a greater variety of parameters that are relevant for gravity waves. Observations of light to moderate CAT and a Kelvin Helmholtz wave at flight altitude confirm the crucial role of non-orographic gravity waves in modulating the ambient airflow and supporting Kelving Helmholtz waves, turbulence, and thus a cascading of kinetic energy from larger to smaller scales.

Table 1
Zonal, Meridional, and Vertical Wave Energy Fluxes EF_x, EF_y, and EF_z Together With Further Quantities Along the Northernmost Sections of Leg 2 and 3 (Each 340 km in Length) of ST10 Calculated From 10 Hz BAHAMAS Data

	EF_x W m^{-2}	EF_y W m^{-2}	EF_z W m^{-2}	$-U\cdot MF$ W m^{-2}	MF_x mPa	MF_y mPa
Leg 2	−10.6	−4.8	0.30	1.63	−41.4	−8.5
Leg 3	−6.0	−7.4	0.16	0.38	−2.9	−24.0

Note. Further quantities computed along these sections are the zonal and meridional momentum fluxes MF_x and MF_y as well as the scalar product of the horizontal wind vector **U** with the horizontal momentum flux **MF** (from Dörnbrack, Bechtold, & Schumann, 2022).

4.5. Wave Analysis

In order to quantify the wave properties at flight level, two about 1,000 km long sections are analyzed. These sections are outermost parts of the long outbound leg 2 and inbound leg 3 of ST10 according to Table S1 of Dörnbrack, Bechtold, and Schumann (2022). Their southernmost way points are at 44.0°S, 63.2°W and 44.6°S, 63.9°W, respectively (compare Figure 3, right column). Thus, these sections reach ∼300 km further to the south-west than the sections shown in Figures 4, 9, and 10 but are otherwise practically identical. The outbound leg 2 was flown at about 12.5 km altitude, the inbound leg 3 at 13.0 km altitude, respectively (see Figure 3).

In the following, we present the three components of the wave energy flux vector $EF_x = u' \cdot p_c'$, $EF_y = v' \cdot p_c'$, and $EF_z = w' \cdot p_c'$, where p_c is the observed static pressure p corrected to a constant reference altitude z_{ref} assuming hydrostatic balance according to $p_c(z) = p(z) + \rho \cdot g \cdot (z - z_{ref})$. Here, z is the aircraft geometric altitude determined from the global positioning system (GPS) and ρ the leg-averaged density as discussed by Smith et al. (2008, 2016). In general, the wave energy flux vector determines in which direction and at which rate energy is being transported by the wave motion (J. A. Dutton, 1976, Section 12.4.3). According to Lindzen (1990), it is the contribution of the pressure-work term to the total wave energy flux. This approach was applied to the SouthTRAC data by Dörnbrack, Bechtold, and Schumann (2022). For this purpose, the 1,000 km legs are divided into three equal sections, each about 340 km in length. Table 1 lists the horizontal and vertical wave energy fluxes for the both northernmost sections (i.e., the second half of panels shown in the left column of Figure 9). The vertical energy fluxes EF_z are positive, the zonal and meridional wave energy fluxes EF_x and EF_y are negative. First of all, these numbers indicate gravity waves propagating vertically upward and traveling against the mean flow. Second, all wave energy fluxes have small values compared to those achieved over mountains that normally exceed 2 W m^{-2} for EF_z and −100 W m^{-2} for EF_x or EF_y (Dörnbrack, Bechtold, & Schumann, 2022; Kruse & Smith, 2015). This finding is consistent with the analyses of Hendricks et al. (2014), who found that gravity waves from spontaneous emission over the southern ocean are much weaker than mountain waves over the Southern Andes. Consistent with the upward propagation of wave energy are the negative vertical fluxes of horizontal momentum MF_x and MF_y.

The wave energy fluxes are relatively small, the magnitude of the MF_x values found here is of the same order of magnitude as the majority of MF_x values observed during the DEEPWAVE campaign above New Zealand (compare Figure 5b in Smith et al., 2016). Furthermore, the reader is reminded of the large scale of the event analyzed here. While the EF_x or EF_y are by more than one order of magnitude smaller when compared with typical mountain waves, the area covered by the event analyzed here is much larger when compared to typical mountain waves. Provided that the energy fluxes found here are representative for the whole area covered by the phase fronts (see Figure 5, right column), we speculate that the associated total energy that is transported per unit time (i.e., the product of energy flux and covered area, in W) is comparable to a more localized mountain wave event.

For a linear, stationary non-dissipative wave the Eliassen-Palm relation predicts that the vertical wave energy flux EF_z equals the negative scalar product of the horizontal wind vector **U** with the momentum flux **MF** (Eliassen & Palm, 1961). The magnitude of this quantity, as listed in the fifth column of Table 1, is always a factor 2 to 5 larger than EF_z which is a possible explanation that the observed gravity waves are not stationary or non-dissipative. This is not a surprising result, but a confirming one, since the forces associated with the strong wind tendencies where the PFJ impinges on the STJ are identified as the source of the waves.

Table 2
Energy Densities KE_x, KE_y, KE_{HP}, KE_z, PE in J m^{-3} As Well As the Dimensionless Ratios $KHR = KE_{HP}/KE_H$, $KER = KE_z/KE_{HP}$, and $EQR = PE/(KE_z + KE_{HP})$ Calculated From 10 Hz BAHAMAS Data

	KE_x	KE_y	KE_{HP}	KE_z	PE	KHR	KER	EQR
Leg 2	0.81	0.49	0.08	0.03	0.83	0.06	0.36	7.59
Leg 3	0.49	2.05	0.05	0.02	0.44	0.02	0.39	5.67

In addition, energy densities are computed along the two northernmost sections of legs 2 and 3 of each 340 km length (Table 2). The energies densities are quadratic quantities (Gill, 1982) and are computed as suggested by Smith et al. (2008, Equations 13–18) but here divided by the length of the respective sections, that is, they are given in J m^{-3}. The KE_x and KE_y components are the squared wind perturbations in the x and y directions and their sum is the horizontal wind energy KE_H. KE_x and KE_y are significantly larger compared to the wave-induced, pressure-corrected horizontal kinetic energy density KE_{HP} as suggested by Smith et al. (2008). KHR is the ratio between

KE_{HP} and KE_H and should be unity in case of no wind layering. Here, we find KHR <<1. The dominance of KE_H is due to large-scale variations of the dynamical variables due to atmospheric processes. KER is the kinetic energy ratio and is close to zero in case of nearly horizontal oscillations by the air parcels and if the waves are nearly hydrostatic. Interestingly, KE_{HP} and the vertical kinetic energy KE_Z have the same order of magnitude, but KE_{HP} is always larger than KE_Z, leading to a ratio KER <1. These results indicate that horizontal air parcel orbits dominate the measured gravity waves, suggesting upward propagating inertial gravity waves as the ones that are detected at flight level.

EQR is the equipartion ratio according to Appendix A of Smith et al. (2008). In linear steady waves, the wave-induced kinetic energy density $KE = (KE_z + KE_{HP})$ should balance the potential energy density PE resulting in an equipartition ratio EQR = 1. Here, EQR is considerably larger than 1. This result is in very good agreement with the values as shown in Figure 14 of Smith et al. (2008). There, the large EQR values could be explained by partial wave reflection in the lower stratospheric levels. It is probably the shorter waves that are reflected in these layers as shown by the spectral analysis presented next.

Figure 11 shows the binned power spectra of the horizontal and vertical wind components *u* and *v* as well as those of the zonal and meridional momentum fluxes MF_x and MF_y for the two outermost sections of the legs 2 and 3 that are about 1,000 km in length. It is known from other aircraft measurements (Kruse & Smith, 2015) that the spectra of the horizontal wind components are dominated by gravity waves longer than about 100 km. The same is true for our measurements. Only in the *v* spectra there is a peak with lower amplitude around 20 km. The power of the *w* spectrum is mainly in the wavelength range between 10 and 50 km. The remarkable result here is the lone peak in vertical power at 2 km horizontal wavelength, which is related to the instability that led to the CAT event associated with the Kelvin-Helmholtz wave. This peak is present in leg 2 of ST10, but it is absent when HALO passes this region again about 45 min later along leg 3, indicating the intermittent, erratic nature of the turbulence encountered. The absence of the peak at 2 km could also be due to the slightly higher flight level, suggesting that the turbulence event is vertically confined, a typical property of sporadically occurring Kelvin-Helmholtz billows. For both analyzed legs, horizontal momentum is mainly transported vertically by gravity waves longer than 100 km and by waves at horizontal wavelengths between 10 and 30 km in zonal direction and 10 and 70 km in meridional direction. The vertical wind spectra clearly indicate the existence of the short-wave instability at 2 km and suggest enhanced but small w-variances due to the turbulence encounter at scales smaller than 1 km.

5. Discussion and Conclusions

Airborne observations combining the remote sensors GLORIA and ALIMA with the in situ sensor BAHAMAS at 100 Hz allowed us to resolve mesoscale fine structures of non-orographic gravity waves, Kelvin-Helmholtz waves and turbulence during a merger of the PFJ with the STJ. With regard to the research questions formulated in the introduction, our conclusions are as follows: the timing, location and alignment of phase lines by the observed non-orographic gravity waves are reproduced well by 1-hourly deterministic short-term forecasts of the IFS at ∼9 km horizontal resolution. Their amplitudes in ΔT are notably smaller when compared to typical orographic gravity waves. In the temporal evolution in the IFS data, elongated phase fronts stretching along more than 3,000 km in horizontal direction are found. They are excited by a jet stream merger at a highly sheared tropopause fold where the PFJ impinges the STJ. The non-orographic gravity waves modulate the static stability in regions with locally enhanced wind shear. In the same regions, Kelvin-Helmholtz waves and CAT are observed. Ten hours before the time of the observations, the IFS data show an X-shaped pattern of phase lines that point upward into the stratosphere and downward into the troposphere. To our best knowledge, such a phase line pattern in connection with a tropospheric jet stream merging event has not been documented before.

According to Vadas and Fritts (2001), spatially confined body forces in the atmosphere result in mean responses and, if the body force is localized enough in space and intermittent enough in time, in the creation of gravity waves. The body-force mechanism for the generation of secondary waves in wave breaking regions was proposed by Vadas et al. (2003). According to Vadas and Becker (2018) and Vadas et al. (2018), characteristic "fish-bone" patterns are found in temperature perturbations due to secondary gravity waves and propagate upward and downward, and forward and backward away from the force. These gravity waves are excited by local body

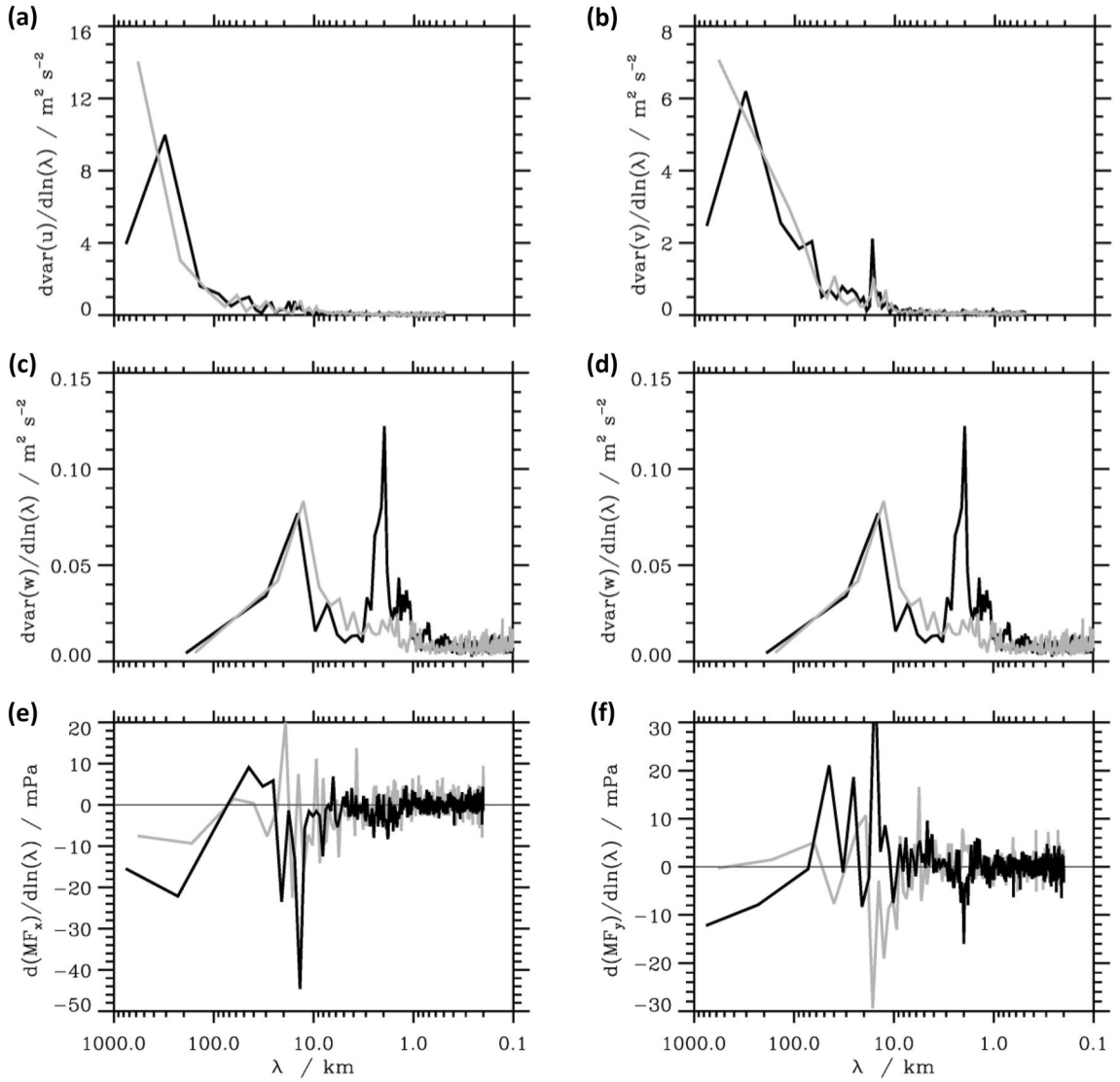

Figure 11. Binned power spectra of the zonal and meridional wind components (upper row), the vertical wind component (middle row, both panels are equal), and the zonal and meridional momentum fluxes (bottom row) as derived from the BAHAMAS data. The black curves are for the outbound leg 2, the gray curves for the inbound leg 3 flown along the same flight track as leg 2. Both analyzed legs are about 1,000 km long.

forces generated by a primary gravity wave. Thereby, the acting force is a horizontal acceleration of the background flow, generated by the dissipation from the primary wave. Becker et al. (2022) furthermore reported partly "X-shaped" patterns of gravity waves excited by spontaneous emission and that they should bear some similarities with gravity waves resulting from local body forces.

In our case study, the analysis of tendencies in the horizontal wind components shows strong deceleration in the zonal direction and acceleration in meridional direction as the PFJ impinges the STJ. The tendencies show that the enhanced tendencies due to the merging of the jet streams act exactly at the source region of the non-orographic gravity waves, that is, the center of the analyzed X-shaped structure. Thereby, the X-shaped structure of the phase lines is not generated by breaking of a primary wave, but by spontaneous generation due to the imbalance of a quasi-geostrophic flow (see Plougonven & Zhang, 2014; references therein). As discussed by Bossert et al. (2020) and in Becker et al. (2022), analogies exist between the body-force mechanism and generation due to spontaneous emission by an unbalanced quasi-geostrophic flow. However, a corresponding mathematical description is not yet available for the latter case.

Moist processes are known to play an important role for gravity waves in baroclinic jet-front systems, resulting in a faster growth, earlier emerging, and larger amplitudes gravity waves which are fully coupled with dry modes (Wei & Zhang, 2014). Moist processes possibly play a role in the study presented here, but are not accessible to the observations and analysis here. Note however that GLORIA observed clouds in the vicinity of the tropopause fold (see high cut-off altitude in the GLORIA data in the troposphere due to clouds after 2,950 km in Figures 4a and 4c), thus supporting that moist processes might play a role here.

The analysis of zonal, meridional, and vertical wave energy and momentum fluxes based on the BAHAMAS data confirm that the probed portion of the non-orographic gravity waves propagates vertically upward and travels against the mean flow. The associated local wave energy fluxes and momentum fluxes are small when compared to those of typical, locally more confined mountain waves. However, provided that the conditions found in the section probed by the observations are representative for the large area covered by the phase fronts seen in the IFS data, such events might contribute significantly to energy redistribution in the upper troposphere and lower stratosphere. The spectra of the horizontal wind components are dominated by wavelengths larger than 100 km, while the power of the w spectrum is mainly in the wavelength range between 10 and 50 km (for details of the analysis of the BAHAMAS data, see Dörnbrack, Bechtold, & Schumann, 2022). A developed lone peak is clearly and consistently identified in vertical power at 2 km horizontal wavelength and corresponds with the instability that led to the CAT event associated with the Kelvin Helmholtz wave.

As shown by the IFS data, the modulation of static stability by the non-orographic gravity waves and tilted bands of locally enhanced shear between the merging jet streams result in patches of low Richardson numbers that are supportive for CAT. Consistently, episodes of light-to-moderate CAT (compare Bramberger et al., 2018, 2020) and Kelvin Helmholtz waves are observed at flight altitude in the 100 Hz BAHAMAS data in these regions. This suggests that the potential for such turbulence events is well accessible to established turbulence forecasting (e.g., Sharman et al., 2012, and references therein).

Conflict of Interest

The authors declare no conflicts of interest relevant to this study.

Data Availability Statement

The GLORIA, ALIMA and BAHAMAS observations and the ECMWF IFS data are available at DOI: https://doi.org/10.5445/IR/1000151856 (Woiwode et al., 2022). For the ECMWF data, the terms of use by the ECMWF apply. ECMWF data are furthermore available at https://www.ecmwf.int/en/forecasts. HYSPLIT trajectories are available via the READY website by the NOAA (https://www.ready.noaa.gov; NOAA, 2022).

Acknowledgments
The authors gratefully acknowledge the Federal Ministry of Education and Research of Germany (BMBF), which supported this study within the research initiative ROMIC II (project WASCLIM, Grants 01LG1907A, 01LG1907D and 01LG1907E). We would like to thank the German Research Foundation (Deutsche Forschungsgemeinschaft, DFG project number 316646266) for funding parts of the SouthTRAC mission costs within the HALO SPP 1294. The authors especially acknowledge the SouthTRAC coordination and flight-planning teams, the GLORIA team from KIT and FZJ, the ALIMA team from DLR-IPA, and the DLR-FX team for planning and carrying out the flights and providing the observations. We thank the ECMWF for providing the meteorological data. Access to the operational ECMWF data was granted through the special project "Gravity Waves and Turbulence over the Andes" by AD. The authors thank the NOAA Air Resources Laboratory (ARL) for the provision of the HYSPLIT transport and dispersion model and READY website (https://www.ready.noaa.gov) used in this publication. Open Access funding enabled and organized by Projekt DEAL.

References

Becker, E., Vadas, S. L., Bossert, K., Harvey, V. L., Zülicke, C., & Hoffmann, L. (2022). A high-resolution whole-atmosphere model with resolved gravity waves and specified large-scale dynamics in the troposphere and stratosphere. *Journal of Geophysical Research: Atmospheres*, *127*(2), e2021JD035018. https://doi.org/10.1029/2021JD035018

Bland, J., Gray, S., Methven, J., & Forbes, R. (2021). Characterising extratropical near-tropopause analysis humidity biases and their radiative effects on temperature forecasts. *Quarterly Journal of the Royal Meteorological Society*, *147*(741), 3878–3898. https://doi.org/10.1002/qj.4150

Bossert, K., Vadas, S. L., Hoffmann, L., Becker, E., Harvey, V. L., & Bramberger, M. (2020). Observations of stratospheric gravity waves over Europe on 12 January 2016: The role of the polar night jet. *Journal of Geophysical Research: Atmospheres*, *125*(21), e2020JD032893. https://doi.org/10.1029/2020JD032893

Bramberger, M., Dörnbrack, A., Wilms, H., Ewald, F., & Sharman, R. (2020). Mountain-wave turbulence encounter of the research aircraft HALO above Iceland. *Journal of Applied Meteorology and Climatology*, *59*(3), 567–588. https://doi.org/10.1175/JAMC-D-19-0079.1

Bramberger, M., Dörnbrack, A., Wilms, H., Gemsa, S., Raynor, K., & Sharman, R. (2018). Vertically propagating mountain waves—A hazard for high-flying aircraft? *Journal of Applied Meteorology and Climatology*, *57*(9), 1957–1975. https://doi.org/10.1175/JAMC-D-17-0340.1

Browning, K., Watkins, C., Starr, J., & McPherson, A. (1970). Simultaneous measurements of clear air turbulence at the tropopause by high-power radar and instrumented aircraft. *Nature*, *228*(5276), 1065–1067. https://doi.org/10.1038/2281065a0

Chilson, P. B., Muschinski, A., & Schmidt, G. (1997). First observations of Kelvin-Helmholtz billows in an upper level jet stream using VHF frequency domain interferometry. *Radio Science*, *32*(3), 1149–1160. https://doi.org/10.1029/97RS00088

Dörnbrack, A. (2021). Stratospheric mountain waves trailing across Northern Europe. *Journal of the Atmospheric Sciences*, *78*(9), 2835–2857. https://doi.org/10.1175/JAS-D-20-0312.1

Dörnbrack, A., Bechtold, P., & Schumann, U. (2022). High-resolution aircraft observations of turbulence and waves in the free atmosphere and comparison with global model predictions. *Journal of Geophysical Research: Atmospheres*, *127*(16), e2022JD036654. https://doi.org/10.1029/2022JD036654

Dörnbrack, A., Eckermann, S. D., Williams, B. P., & Haggerty, J. (2022). Stratospheric gravity waves excited by propagating Rossby wave trains – A DEEPWAVE case study. *Journal of the Atmospheric Sciences*, *79*(2), 567–591. https://doi.org/10.1175/JAS-D-21-0057.1

Dörnbrack, A., Gisinger, S., Kaifler, N., Portele, T. C., Bramberger, M., Rapp, M., et al. (2018). Gravity waves excited during a minor sudden stratospheric warming. *Atmospheric Chemistry and Physics*, *18*(17), 12915–12931. https://doi.org/10.5194/acp-18-12915-2018

Dörnbrack, A., Kaifler, B., Kaifler, N., Rapp, M., Wildmann, N., Garhammer, M., et al. (2020). Unusual appearance of mother-of-pearl clouds above El Calafate, Argentina (50° 21′ S, 72° 16′ W). *Weather*, *75*(12), 378–388. https://doi.org/10.1002/wea.3863

Draxler, R. R., & Hess, G. D. (1998). An overview of the HYSPLIT_4 modeling system of trajectories, dispersion, and deposition. *Australian Meteorological Magazine*, *47*, 295–308.

Dutton, J. A. (1976). *The ceaseless wind* (1st ed., p. 579). McGraw-Hill.

Dyroff, C., Zahn, A., Christner, E., Forbes, R., Tompkins, A. M., & van Velthoven, P. F. J. (2015). Comparison of ECMWF analysis and forecast humidity data with CARIBIC upper troposphere and lower stratosphere observations. *The Quarterly Journal of the Royal Meteorological Society*, *141*(688), 833–844. https://doi.org/10.1002/qj.2400

Ehard, B., Kaifler, B., Kaifler, N., & Rapp, M. (2015). Evaluation of methods for gravity wave extraction from middle-atmospheric lidar temperature measurements. *Atmospheric Measurement Techniques*, *8*(11), 4645–4655. https://doi.org/10.5194/amt-8-4645-2015

Eliassen, A., & Palm, E. (1961). On the transfer of energy in stationary mountain waves. *Geofysiske Publikasjoner*, *22*(3), 1–23.

Friedl-Vallon, F., Gulde, T., Hase, F., Kleinert, A., Kulessa, T., Maucher, G., et al. (2014). Instrument concept of the imaging Fourier transform spectrometer GLORIA. *Atmospheric Measurement Techniques*, *7*(10), 3565–3577. https://doi.org/10.5194/amt-7-3565-2014

Geldenhuys, M., Kaifler, B., Preusse, P., Ungermann, J., Alexander, P., Krasauskas, L., et al. (2023). Observations of gravity wave refraction and its causes and consequences. *Journal of Geophysical Research: Atmospheres*, *128*(3), e2022JD036830. https://doi.org/10.1029/2022JD036830

Gettelman, A., Hoor, P., Pan, L. L., Randel, W. J., Hegglin, M. I., & Birner, T. (2011). The extratropical upper troposphere and lower stratosphere. *Review of Geophysics*, *49*(3), RG3003. https://doi.org/10.1029/2011RG000355

Giez, A., Mallaun, C., Nenakhov, V., & Zöger, M. (2021). *Calibration of a nose boom mounted airflow sensor on an atmospheric research aircraft by inflight maneuvers (Technical report no. 2021-17)*. DLR. Retrieved from https://elib.dlr.de/145969/

Giez, A., Mallaun, C., Zöger, M., Dörnbrack, A., & Schumann, U. (2017). Static pressure from aircraft trailing-cone measurements and numerical weatherprediction analysis. *Journal of Aircraft*, *54*(5), 1728–1737. https://doi.org/10.2514/1.C034084

Giez, A., Zöger, M., Dreiling, V., & Mallaun, C. (2019). Static source error calibration of a nose boom mounted air data system on an atmospheric research aircraft using the trailing cone method. *DLR Internal Report, 2019-07*, 87.

Giez, A., Zöger, M., Mallaun, C., Nenakhov, V., Schimpf, M., Grad, C., et al. (2023). *Determination of the measurement errors for the HALO basic data system BAHAMAS by means of error propagation*. DLR-Forschungsbericht, DLR-FB-2022-27. (p. 97). https://doi.org/10.57676/5rdc-q708

Gill, A. E. (1982). *Atmosphere–Ocean dynamics* (p. 662). Academic Press.

Gisinger, S., Polichtchouk, I., Dörnbrack, A., Reichert, R., Kaifler, B., Kaifler, N., et al. (2022). Gravity-wave-driven seasonal variability of temperature differences between ECMWF IFS and Rayleigh lidar measurements in the lee of the Southern Andes. *Journal of Geophysical Research: Atmospheres*, *127*(13), e2021JD036270. https://doi.org/10.1029/2021JD036270

Gupta, A., Birner, T., Dörnbrack, A., & Polichtchouk, I. (2021). Importance of gravity wave forcing for springtime southern polar vortex breakdown as revealed by ERA5. *Geophysical Research Letters*, *48*(10), e2021GL092762. https://doi.org/10.1029/2021GL092762

Hendricks, E. A., Doyle, J. D., Eckermann, S. D., Jiang, Q., & Reinecke, P. A. (2014). What is the source of the stratospheric gravity wave belt in austral winter? *Journal of the Atmospheric Sciences*, *71*(5), 1583–1592. https://doi.org/10.1175/JAS-D-13-0332.1

Hersbach, H., Bell, B., Berrisford, P., Hirahara, S., Horanyi, A., Munoz-Sabater, J., et al. (2020). The ERA5 global reanalysis. *The Quarterly Journal of the Royal Meteorological Society*, *146*(730), 1999–2049. https://doi.org/10.1002/qj.3803

Hertzog, A., Boccara, G., Vincent, R., Vial, F., & Coquerez, P. (2008). Estimation of gravity-wave momentum fluxes and phase speeds from long-duration stratospheric balloon flights. 2. Results from the Vorcore campaign in Antarctica. *Journal of the Atmospheric Sciences*, *65*(10), 3056–3070. https://doi.org/10.1175/2008jas2710.1

Hólm, E., Forbes, R., Lang, S., Magnusson, L., & Malardel, S. (2016). *New model cycle brings higher resolution* (Vol. 147, pp. 14–19). ECMWF Newsletter.

ICAO. (2001). *Meteorological service for international air navigation. Annex 3 to the Convention on International Civil Aviation* (14th ed., p. 128). International Civil Aviation Organization Doc.

Johansson, S., Woiwode, W., Höpfner, M., Friedl-Vallon, F., Kleinert, A., Kretschmer, E., et al. (2018). Airborne limb-imaging measurements of temperature, HNO_3, O_3, $ClONO_2$, H_2O and CFC-12 during the Arctic winter 2015/2016: Characterization, in situ validation and comparison to Aura/MLS. *Atmospheric Measurement Techniques*, *11*(8), 4737–4756. https://doi.org/10.5194/amt-11-4737-2018

Kaifler, B., & Kaifler, N. (2021). A Compact Rayleigh Autonomous lidar (CORAL) for the middle atmosphere. *Atmospheric Measurement Techniques*, *14*(2), 1715–1732. https://doi.org/10.5194/amt-14-1715-2021

Kennedy, P. J., & Shapiro, M. A. (1975). The energy budget in a clear air turbulence zone as observed by aircraft. *Monthly Weather Review*, *103*(7), 650–654. https://doi.org/10.1175/1520-0493(1975)103,0650:TEBIAC.2.0.CO;2

Knox, J. A. (1997). Possible mechanisms of clear-air turbulence in strongly anticyclonic flows. *Monthly Weather Review*, *125*(6), 1251–1259. https://doi.org/10.1175/1520-0493(1997)125<1251:PMOCAT>2.0.CO;2

Knox, J. A., McCann, D. W., & Williams, P. D. (2008). Application of the Lighthill–Ford theory of spontaneous imbalance to clear-air turbulence forecasting. *Journal of the Atmospheric Sciences*, *65*(10), 3292–3304. https://doi.org/10.1175/2008JAS2477.1

Koch, S. E., Jamison, B. D., Lu, C. G., Smith, T. L., Tollerud, E. I., Girz, C., et al. (2005). Turbulence and gravity waves within an upper-level front. *Journal of the Atmospheric Sciences*, *62*(11), 3885–3908. https://doi.org/10.1175/Jas3574.1

Krasauskas, L., Kaifler, B., Rhode, S., Ungermann, J., Woiwode, W., & Preusse, P. (2022). Oblique propagation of mountain waves to the upwind side of the Andes observed by GLORIA and ALIMA during the SouthTRAC campaign. *Authorea*, September 07, 2022. https://doi.org/10.1002/essoar.10512325.1

Krasauskas, L., Ungermann, J., Preusse, P., Friedl-Vallon, F., Zahn, A., Ziereis, H., et al. (2021). 3-D tomographic observations of Rossby wave breaking over the North Atlantic during the WISE aircraft campaign in 2017. *Atmospheric Chemistry and Physics*, *21*(13), 10249–10272. https://doi.org/10.5194/acp-21-10249-2021

Krautstrunk, M., & Giez, A. (2012). The transition from FALCON to HALO era airborne atmospheric research. In U. Schumann (Ed.), *Atmospheric physics*, *Research topics in aerospace* (pp. 609–624). Springer Verlag. https://doi.org/10.1007/978-3-642-30183-4_37

Krisch, I., Preusse, P., Ungermann, J., Dörnbrack, A., Eckermann, S. D., Ern, M., et al. (2017). First tomographic observations of gravity waves by the infrared limb imager GLORIA. *Atmospheric Chemistry and Physics*, *17*(24), 14937–14953. https://doi.org/10.5194/acp-17-14937-2017

Kruse, C. G., & Smith, R. B. (2015). Gravity wave diagnostics and characteristics in mesoscale fields. *Journal of the Atmospheric Sciences*, *72*(11), 4372–4392. https://doi.org/10.1175/JAS-D-15-0079.1

Lim, E., Hendon, H. H., Butler, A. H., Thompson, D. W. J., Lawrence, Z. D., Scaife, A. A., et al. (2021). The 2019 southern hemisphere stratospheric polar vortex weakening and its impacts. *Bulletin of the American Meteorological Society*, *102*(6), E1150–E1171. https://doi.org/10.1175/BAMS-D-20-0112.1

Lindzen, R. S. (1990). *Dynamics in atmospheric physics* (p. 310). Cambridge University Press.

Magnusson, L., Chen, J.-H., Lin, S.-J., Zhou, L., & Chen, X. (2019). Dependence on initial conditions versus model formulations for medium-range forecast error variations. *Quarterly Journal of the Royal Meteorological Society*, *145*(722), 2085–2100. https://doi.org/10.1002/qj.3545

Malardel, S., & Wedi, N. P. (2016). How does subgrid-scale parametrization influence nonlinear spectral energy fluxes in global NWP models? *Journal of Geophysical Research-Atmosphere*, *121*(10), 5395–5410. https://doi.org/10.1002/2015JD023970

Mauritsen, T., & Svensson, G. (2007). Observations of stably stratified shear-driven atmospheric turbulence at low and high Richardson numbers. *Journal of the Atmospheric Sciences*, *64*(2), 645–655. https://doi.org/10.1175/JAS3856.1

Morgan, M. C., & Nielsen-Gammon, J. W. (1998). Using tropopause maps to diagnose midlatitude weather systems. *Monthly Weather Review*, *126*(10), 2555–2579. https://doi.org/10.1175/1520-0493(1998)126<2555:utmtdm>2.0.co;2

NOAA. (2022). *READY Real-time Environmental Applications and Display sYstem*. NOAA Air Resources Laboratory. Retrieved from https://www.ready.noaa.gov

O'Sullivan, D., & Dunkerton, T. J. (1995). Generation of inertia–gravity waves in a simulated life cycle of baroclinic instability. *Journal of the Atmospheric Sciences*, *52*(21), 3695–3716. https://doi.org/10.1175/1520-0469(1995)052<3695:GOIWIA>2.0.CO;2

Panofsky, H. A., Dutton, J. A., Hemmerich, K. H., McCreary, G., & Loving, N. V. (1968). Case studies of the distribution of CAT in the troposphere and stratosphere. *Journal of Applied Meteorology and Climatology*, *7*(3), 384–389. https://doi.org/10.1175/1520-0450(1968)007⟨0384:CSOTDO⟩2.0.CO;2

Plougonven, R., Hertzog, A., & Guez, L. (2013). Gravity waves over Antarctica and the Southern Ocean: Consistent momentum fluxes in mesoscale simulations and stratospheric balloon observations. *Quarterly Journal of the Royal Meteorological Society*, *139*(670), 101–118. https://doi.org/10.1002/qj.1965

Plougonven, R., & Teitelbaum, H. (2003). Comparison of a large-scale inertia-gravity wave as seen in the ECMWF analyses and from radiosondes. *Geophysical Research Letters*, *30*(18), 1954. https://doi.org/10.1029/2003GL017716

Plougonven, R., & Zhang, F. (2014). Internal gravity waves from atmospheric jets and fronts. *Review of Geophysics*, *52*(1), 33–76. https://doi.org/10.1002/2012RG000419

Plougonven, R., & Zhang, F. (2016). Gravity waves generated by jets and fronts and their relevance for clear-air turbulence. In *Aviation turbulence* (pp. 385–406). Springer International Publishing.

Rapp, M., Kaifler, B., Dörnbrack, A., Gisinger, S., Mixa, T., Reichert, R., et al. (2021). SOUTHTRAC-GW: An airborne field campaign to explore gravity wave dynamics at the world's strongest hotspot. *Bulletin of the American Meteorological Society*, *102*(4), E871–E893. https://doi.org/10.1175/BAMS-D-20-0034.1

Riese, M., Oelhaf, H., Preusse, P., Blank, J., Ern, M., Friedl-Vallon, F., et al. (2014). Gimballed Limb Observer for Radiance Imaging of the Atmosphere (GLORIA) scientific objectives. *Atmospheric Measurement Techniques*, *7*, 1915–1928. https://doi.org/10.5194/amt-7-1915-2014

Rodriguez Imazio, P., Dörnbrack, A., Urzua, R. D., Rivaben, N., & Godoy, A. (2022). Clear air turbulence observed across a tropopause fold over the Drake passage - A case study. *Journal of Geophysical Research: Atmospheres*, *127*(4), e2021JD035908. https://doi.org/10.1029/2021JD035908

Sato, K., Watanabe, S., Kawatani, Y., Tomikawa, Y., Miyazaki, K., & Takahashi, M. (2009). On the origins of mesospheric gravity waves. *Geophysical Research Letters*, *36*(19), L19801. https://doi.org/10.1029/2009GL039908

Shapiro, M. A. (1980). Turbulent mixing within tropopause folds as a mechanism for the exchange of chemical-constituents between the stratosphere and troposphere. *Journal of the Atmospheric Sciences*, *37*(5), 994–1004. https://doi.org/10.1175/1520-0469(1980)037<0994:tmwtfa>2.0.co;2

Sharman, R. D., Cornman, L. B., Meymaris, G., Pearson, J., & Farrar, T. (2014). Description and derived climatologies of Automated in situ eddy-dissipation-rate reports of atmospheric turbulence. *Journal of Applied Meteorology and Climatology*, *53*(6), 1416–1432. https://doi.org/10.1175/JAMC-D-13-0329.1

Sharman, R. D., Trier, S. B., Lane, T. P., & Doyle, J. D. (2012). Sources and dynamics of turbulence in the upper troposphere and lower stratosphere: A review. *Geophysical Research Letters*, *39*(12), L12803. https://doi.org/10.1029/2012GL051996

Smalikho, I. N. (1997). Accuracy of the turbulent energy dissipation rate estimation from the temporal spectrum of wind velocity fluctuations. *Atmospheric and Oceanic Optics*, *10*(8), 559–563.

Smith, R. B., Nugent, A. D., Kruse, C. G., Fritts, D. C., Doyle, J. D., Eckermann, S. D., et al. (2016). Stratospheric gravity wave fluxes and scales during DEEPWAVE. *Journal of the Atmospheric Sciences*, *73*(7), 2851–2869. https://doi.org/10.1175/JAS-D-15-0324.1

Smith, R. B., Woods, B. K., Jensen, J., Cooper, W. A., Doyle, J. D., Jiang, Q., & Grubišić, V. (2008). Mountain waves entering the stratosphere. *Journal of the Atmospheric Sciences*, *65*(8), 2543–2562. https://doi.org/10.1175/2007JAS2598.1

Stein, A. F., Draxler, R. R., Rolph, G. D., Stunder, B. J. B., Cohen, M. D., & Ngan, F. (2015). NOAA's HYSPLIT atmospheric transport and dispersion modeling system. *Bulletin of the American Meteorological Society*, *96*(12), 2059–2077. https://doi.org/10.1175/BAMS-D-14-00110.1

Stenke, A., Grewe, V., & Ponater, M. (2008). Lagrangian transport of water vapour and cloud water in the ECHAM4 GCM and its impact on the cold bias. *Climate Dynamics*, *31*(5), 491–506. https://doi.org/10.1007/s00382-007-0347-5

Strauss, L., Serafin, S., Haimov, S., & Grubii, V. (2015). Turbulence in breaking mountain waves and atmospheric rotors estimated from airborne in situ and Doppler radar measurements. *Quarterly Journal of Royal Meteorological Society*, *141*(693), 3207–3225. https://doi.org/10.1002/qj.2604

Teixeira, M. A. C. (2014). The physics of orographic gravity wave drag. *Frontiers in Physics*, *2*. https://doi.org/10.3389/fphy.2014.00043

Ungermann, J., Blank, J., Lotz, J., Leppkes, K., Hoffmann, L., Guggenmoser, T., et al. (2011). A 3-D tomographic retrieval approach with advection compensation for the air-borne limb-imager GLORIA. *Atmospheric Measurement Techniques*, *4*(11), 2509–2529. https://doi.org/10.5194/amt-4-2509-2011

Ungermann, J., Kleinert, A., Maucher, G., Bartolomé, I., Friedl-Vallon, F., Johansson, S., et al. (2022). Quantification and mitigation of the instrument effects and uncertainties of the airborne limb imaging FTIR GLORIA. *Atmospheric Measurement Techniques*, *15*(8), 2503–2530. https://doi.org/10.5194/amt-15-2503-2022

Vadas, S. L., & Becker, E. (2018). Numerical modeling of the excitation, propagation, and dissipation of primary and secondary gravity waves during wintertime at McMurdo Station in the Antarctic. *Journal of Geophysical Research: Atmospheres*, *123*(17), 9326–9369. https://doi.org/10.1029/2017JD027974

Vadas, S. L., & Fritts, D. C. (2001). Gravity wave radiation and mean responses to local body forces in the atmosphere. *Journal of the Atmospheric Sciences*, *58*(16), 2249–2279. https://doi.org/10.1175/1520-0469(2001)058<2249:GWRAMR>2.0.CO;2

Vadas, S. L., Fritts, D. C., & Alexander, M. J. (2003). Mechanism for the generation of secondary waves in wave breaking regions. *Journal of the Atmospheric Sciences*, *60*(1), 194–214. https://doi.org/10.1175/1520-0469(2003)060<0194:MFTGOS>2.0.CO;2

Vadas, S. L., Zhao, J., Chu, X., & Becker, E. (2018). The excitation of secondary gravity waves from local body forces: Theory and observation. *Journal of Geophysical Research: Atmospheres*, *123*(17), 9296–9325. https://doi.org/10.1029/2017JD027970

Wei, J., & Zhang, F. (2014). Mesoscale gravity waves in moist baroclinic jet–front systems. *Journal of the Atmospheric Sciences*, *71*(3), 929–952. https://doi.org/10.1175/JAS-D-13-0171.1

Wetzel, G., Friedl-Vallon, F., Glatthor, N., Grooß, J.-U., Gulde, T., Höpfner, M., et al. (2021). Pollution trace gases C_2H_6, C_2H_2, HCOOH, and PAN in the North Atlantic UTLS: Observations and simulations. *Atmospheric Chemistry and Physics*, *21*(10), 8213–8232. https://doi.org/10.5194/acp-21-8213-2021

Woiwode, W., Dörnbrack, A., Bramberger, M., Friedl-Vallon, F., Haenel, F., Höpfner, M., et al. (2018). Mesoscale fine structure of a tropopause fold over mountains. *Atmospheric Chemistry and Physics*, *18*(21), 15643–15667. https://doi.org/10.5194/acp-18-15643-2018

Woiwode, W., Dörnbrack, A., Johansson, S., Kaifler, B., & Giez, A. (2022). GLORIA, ALIMA, BAHAMAS and ECMWF IFS data for South-TRAC flight 10 from 16 to 17 September 2019. [Dataset]. KITopen. https://doi.org/10.5445/IR/1000151856

Woiwode, W., Dörnbrack, A., Polichtchouk, I., Johansson, S., Harvey, B., Höpfner, M., et al. (2020). Technical note: Lowermost-stratosphere moist bias in ECMWF IFS model diagnosed from airborne GLORIA observations during winter–spring 2016. *Atmospheric Chemistry and Physics*, *20*(23), 15379–15387. https://doi.org/10.5194/acp-20-15379-2020

Zhang, S. D., & Yi, F. (2005). A statistical study of gravity waves from radiosonde observations at Wuhan (30° N, 114° E) China. *Annales Geophysicae*, *23*(3), 665–673. https://doi.org/10.5194/angeo-23-665-2005

Zhang, S. D., & Yi, F. (2007). Latitudinal and seasonal variations of inertial gravity wave activity in the lower atmosphere over central China. *Journal of Geophysical Research*, *112*(D5), D05109. https://doi.org/10.1029/2006JD007487

Zhang, S. D., Yi, F., Huang, C. M., & Chen, Z. Y. (2008). Intensive radiosonde observations of gravity waves in the lower atmosphere over Yichang (111°18´ E, 30°42´ N), China. *Annales Geophysicae*, *26*(7), 2005. https://doi.org/10.5194/angeo-26-2005-2008